SPATIOTEMPORAL DYNAMICS OF LOW FREQUENCY

FLUCTUATIONS IN BOLD FMRI

A Dissertation
Presented to
The Academic Faculty

by

Waqas Majeed

In Partial Fulfillment
of the Requirements for the Degree
Doctor of Philosophy in
Bioengineering through the
School of Electrical and Computer Engineering

Georgia Institute of Technology
December 2010

SPATIOTEMPORAL DYNAMICS OF LOW FREQUENCY

FLUCTUATIONS IN BOLD FMRI

Approved by:

Dr. Shella Keilholz, Advisor
School of Biomedical Engineering
*Georgia Institute of Technology and
Emory University*

Dr. Xiaoping Hu
School of Biomedical Engineering
*Georgia Institute of Technology and
Emory University*

Dr. Dieter Jaeger
School of Biology
Emory University

Dr. Krish Sathian
School of Neurology
Emory University

Dr. Eric Schumacher
School of Psychology
Georgia Institute of Technology

Date Approved: August 19, 2010

ACKNOWLEDGEMENTS

TABLE OF CONTENTS

LIST OF FIGURES

LIST OF SYMBOLS AND ABBREVIATIONS

BOLD	Blood oxygenation dependent signal
CBV	Cerebral blood volume
cc	Correlation coefficient
CP	Caudate-putamen
fMRI	Functional magnetic resonance imaging
LFFs	Low frequency fluctuations
LFP	Local field potentials
PCC	Posterior Cingulate Cortex
ROI	Region of interest
SI	Primary somatosensory cortex
SII	Secondary somatosensory cortex
T2*	Spin-spin relaxation time-constant
TE	Echo time
TR	Repetition time

SUMMARY

Traditional fMRI utilizes blood oxygenation level dependent (BOLD) contrast to map brain activity. BOLD signal is sensitive to the hemodynamic changes associated with brain activity, and gives an indirect measure of brain activity. Low frequency fluctuations (LFFs) have been observed in the BOLD signal even in the absence of any anesthetic agent, and the correlations between the fluctuations from different brain regions has been used to map functional connectivity in the brain. Most studies involving spontaneous fluctuations in the BOLD signal extract connectivity patterns that show relationships between brain areas that are maintained over the length of the scanning session. The research presented in this document investigates the spatiotemporal dynamics of the BOLD fluctuations to identify common spatiotemporal patterns within a scan, and suggests the presence of multiple contributions to low frequency fluctuations in rats as well as humans. First, the presence of a visually detectable spatiotemporal propagation pattern is demonstrated by utilizing single-slice data with high spatial and temporal resolution. The pattern consists of lateral-medial propagation of BOLD signal, demonstrating the presence of time-varying features in spontaneous BOLD fluctuations. Further, a novel pattern finding algorithm is developed for detecting repeated spatiotemporal patterns in BOLD fMRI data. The algorithm is applied to high temporal resolution T2*-weighted multislice images obtained from rats and humans in the absence of any task or stimulation. In rats, the primary pattern consists of waves of high signal

intensity, propagating in a lateral-medial direction across the cortex, replicating the results obtained using visual observation. In humans, the most common spatiotemporal pattern consisted of an alteration between activation of areas comprising the "default-mode" (e.g., posterior cingulate and anterior medial prefrontal cortices) and the "task-positive" (e.g., superior parietal and premotor cortices) networks. Signal propagation from focal starting points is also observed. The pattern finding algorithm is shown to be reasonably insensitive to the variation in user-defined parameters, and the results are consistent within and between subjects.

This novel approach for probing the spontaneous network activity of the brain has implications for the interpretation of conventional functional connectivity studies, and may increase the amount of information that can be obtained from neuroimaging data.

CHAPTER 1

INTRODUCTION

Functional MRI (fMRI)

There has been steady growth in the popularity of functional MRI (fMRI) since its inception about 20 years ago. Its ability to non-invasively localize functionally active regions of brain with high spatial resolution (~100 microns to 4-5 mm) and moderate temporal resolution (> ~0.1s) makes it an attractive choice for imaging brain function in humans as well as animal models. fMRI does not measure the brain activity directly. Instead, it is sensitive to hemodynamic changes following brain activity. The most common functional imaging method utilizing MRI is BOLD (Blood Oxygenation Level Dependent) fMRI (Ogawa, Lee et al. 1990). It relies on hemoglobin as an intrinsic contrast agent. Oxygenated hemoglobin is diamagnetic, whereas deoxygenated hemoglobin is paramagnetic. Brain activation results in a series of changes involving increased blood flow and volume in the area of activation. These changes are needed to meet the increased metabolic demands of the activated regions. The increase in supply exceeds the demand and the oxygenation level (fraction of oxygenated hemoglobin) in the vicinity of the activated area rises. As a result, magnetic field homogeneity near the activated area is improved and the signal increases in the activated area. Other methods of achieving functional contrast using MRI include cerebral blood flow (CBF) (Ostergaard, Weisskoff et al. 1996) and cerebral blood volume (CBV) (Lu, Golay et al. 2003; Zhao, Wang et al. 2005) weighted imaging.

As stated above, fMRI does not measure brain activity directly. Simultaneous acquisition of BOLD and electrical activity of the brain has been used to investigate the relationship between the BOLD signal and neural activity. Brinker et al. utilized simultaneous recording to demonstrate validity of BOLD fMRI for estimating the electrocortical potentials (Brinker, Bock et al. 1999). Somatosensory evoked potentials (SEP) and T2* weighted MRI images were recorded simultaneously during somatosensory stimulation of rat to investigate the relationship between electrical activation of the brain tissue and the signal intensity change. A linear relationship between the BOLD signal and SEPs was demonstrated. Logothetis et al. utilized simultaneous electrophysiology and fMRI measurements in monkeys in order to demonstrate that local field potentials (LFPs) are better predictors for the BOLD signal as compared with action potentials during visual stimulation. . These studies support the use of fMRI as a valid functional imaging modality.

The majority of fMRI experiments utilize a task-based paradigm. The subject is asked to perform a task involving mental activity, interleaved with periods of rest or a control task. The fMRI signal during the task performance is compared with the signal during rest (baseline) and activation maps are created. Multiple runs are acquired in order to increase signal to noise ratio. Such experiments have been extensively used for functional mapping of brain (Cohen, Forman et al. 1993; Sakai, Watanabe et al. 1995; Kim, Duong et al. 2000).

Low Frequency Fluctuations (LFFs) and Functional connectivity

The first few years of fMRI research were focused on detecting task-induced changes in the BOLD signal, and the fluctuations unrelated to the stimulus were

disregarded as noise. Biswal et al (Biswal, Yetkin et al. 1995) demonstrated the presence of low frequency fluctuations (f < 0.08 Hz) in the fMRI time-courses acquired in absence of any task or stimulus. Strong correlation was observed between the low frequency fluctuations in left and right motor cortices. The correlations were hypothesized to reflect synchronous spontaneous brain activity between the regions showing high correlation. These correlations are referred to as "functional connectivity", and such studies are called "resting state" studies due to absence of any controlled task or stimulus. Since then, there has been explosive growth in the research conducted in this area. Conceptually, functional connectivity analysis aims at finding areas of the brain with synchronized spontaneous fluctuations in the BOLD signal. Those areas are presumed to exhibit synchronized modulations in neural activity, and hence are "functionally connected". This may provide a way to look at brain networks comprising the areas working together non-invasively and has potential applications in both basic and clinical research.

The fcMRI signal is contaminated by scanner noise as well as respiratory and cardiac contributions. Most studies utilize relatively low sampling rates, which result in aliasing of physiological noise. Although it is not a concern for task-based paradigms as averaging can be performed in order to remove the effect of noise, averaging of multiple trials cannot be use for functional connectivity analysis because the spontaneous fluctuations would average out towards zero in addition to the noise. Therefore, part of the correlation observed in functional connectivity maps has non-neural physiological contributions. Physiological noise correction can be performed on the data to reduce these non-neural contributions (Hu, Le et al. 1995; Glover, Li et al. 2000; Birn, Diamond et al. 2006).

The simplest method to measure functional connectivity is to obtain the average time course from a seed region (for example primary motor cortex) and to obtain cross correlation values between the seed regions and all the voxels in the brain. The correlation values are displayed as a "functional connectivity map" or FC map. High correlation values are interpreted as stronger functional connection. This method for mapping functional connectivity is easy to use and implement. However, it requires manual selection of the seed region, which can bias the results and makes automatic exploratory analysis impossible. Another popular method is based upon independent component analysis (ICA). This method aims at finding the independent sources contributing to the time-courses corresponding to voxels in the brain. Contributions of the independent sources are hypothesized to reflect different functional networks. ICA is data driven and therefore does not suffer from the bias due to manual seed selection. Also, it provides a way to retrospectively estimate the components due to noise. However, it generates a large number of components which are not ranked in any order. Therefore, manual inspection of the components and their spatial distributions is necessary in order to select the potentially relevant components. Additionally, the correspondence between the components generated by ICA and actual sources contributing to BOLD signals is not guaranteed.

Many studies aim at identifying functional networks in the brain. Networks associated with different systems including visual, auditory, default mode, memory, language and attention have been identified. (Cordes, Haughton et al. 2000; Hampson, Peterson et al. 2002; Fox, Snyder et al. 2005; Fox, Corbetta et al. 2006). The default mode network in particular has been the subject of many studies.

Default mode network

Certain areas of brain (e.g. posterior cingulate and anterior medial prefrontal cortices) have been observed to decrease their activity during attention demanding cognitive tasks (Raichle, MacLeod et al. 2001). These areas were hypothesized to be involved in important activities that may underlie the baseline state of the human brain (or the "default mode" of brain function) (Raichle, MacLeod et al. 2001). Interestingly, strong correlation exists between LFFs in these areas, and the corresponding network with synchronous LFFs was termed as the "default mode network" (Greicius, Krasnow et al. 2003; Fox, Snyder et al. 2005). Additionally, a network anti-correlated with default mode network was identified (Fox, Snyder et al. 2005). This network includes areas (e.g. superior parietal and premotor cortices) that are active during the performance of a wide variety of tasks and that may be related to attention, and is termed as "task positive" or "attention" network (Fox, Snyder et al. 2005). These networks have been hypothesized to constitute the intrinsic functional architecture of the brain, and have gained immense interest in fMRI and neuroscience communities.

Neural and behavioral significance of LFFs in Humans

Many studies focus on the effect of different treatments and pathological conditions on functional connectivity and LFFs to see if the results are consistent with a neural origin of functional connectivity. Anesthesia, hypercapnia and cocaine administration have been reported to disrupt functional connectivity (Biswal, Hudetz et al. 1997; Li, Biswal et al. 2000; Peltier, Kerssens et al. 2005). Anesthesia and cocaine administration alter neural activity as well as hemodynamics, whereas hypercapnia alters hemodynamics only. Therefore, effects on the functional connectivity observed in these

studies may not be completely attributed to neural activity or vasculature. Changes in functional connectivity have been observed in autism, Alzheimer's disease, multiple sclerosis, depression, schizophrenia, attention deficit hyperactivity disorder, epilepsy and blindness (Grady, Furey et al. 2001; Lowe, Phillips et al. 2002; Villalobos, Mizuno et al. 2005; Garrity, Pearlson et al. 2007; Greicius, Flores et al. 2007; Liu, Yu et al. 2007). As noted above, a common confounding factor for these studies is that the aforementioned diseases and treatments may alter the neurovascular coupling in addition to neural activity.

Other studies suggest functional and behavioral significance of LFFs and functional connectivity. Correlation between a region in the brain and hippocampus has been shown to predict the region's response to episodic memory (Vincent, Snyder et al. 2006). Spatial patterns of functional connectivity have been shown to predict individual differences in pre-scan anxiety and performance on working memory tasks (Seeley, Menon et al. 2007). Seeley et al identified a "salience network" that links dorsal anterior cingulate (dACC) and orbital frontoinsular cortices with subcortical and limbic structures, and an "executive-control network" that links dorsolateral frontal and parietal cortices. Prescan anxiety ratings correlated with functional connectivity of the dACC node of the salience network, but with no region in the executive-control network, whereas executive task performance correlated with lateral parietal nodes of the executive-control network, but with no region in the salience network (Seeley, Menon et al. 2007). These studies suggest that LFFs have functional relevance and may reflect spontaneous activity of the brain.

Other studies provide a more direct evidence of neural basis of LFFs and functional connectivity.. Loss of connectivity between hemispheres has been reported after complete section of corpus callosum (Johnston, Vaishnavi et al. 2008). Intra-hemespheric connectivity was preserved, however. This study suggests that functional connectivity is likely to reflect actual neural connectivity, instead of synchronization between noise contributions. Combined EEG-fMRI studies have been performed in order to investigate the neural basis of LFFs and functional connectivity. Goldman et al reported negative correlation between BOLD and α band power in multiple cortical regions of awake humans using simultaneous acquisition of EEG and fMRI (Goldman, Stern et al. 2002). Another simultaneous EEG-fMRI study by Mantini et al (Mantini, Perrucci et al. 2007) suggests that multiple frequency bands are related to the LFFs, and that the frequency spectra is different for different functional networks. A recently published human study by He et al utilizes electrocorticography and fMRI in the patients with intractable epilepsy and indirectly suggests that both slow cortical potentials (f < 4Hz, overlapping with delta band) and gamma band power are related to LFFs in BOLD in wakefulness and rapid-eye-movement sleep (He, Snyder et al. 2008). Only slow cortical potentials showed a correlation pattern similar to that of LFFs in other states of sleep. In another study, the spatial pattern of correlation between BOLD fluctuations and the power of alpha rhythm varied within and between the subjects, suggesting that the relationship between LFFs and the EEG signal may vary depending on the current state of the subject (Gonçalves, de Munck et al. 2006). These studies suggest the link between LFFs in BOLD and electrical activity in the brain. In general, the area of the brain that is studied, the relative sensitivity of the electrical recording techniques, and the state of the

subject (awake, asleep, or anesthetized) might explain some of the differences in the findings. Most experiments on humans are performed without anesthesia. Significant inter-subject variability can be expected due to individual differences in mood, personality, background thoughts, use of medication / other agents affecting connectivity (e.g. caffeine) and scanner anxiety. These studies highlight the need for further research addressing the issue of the neural origin of the LFFs in BOLD. Another issue with these studies is the low spectral resolution for BOLD fMRI data due to long TRs (~1.5-3s, required for whole brain coverage), as well as small number of repetitions (< 500, needed to reduce the time required for data acquisition). There might be different neural origins for different sub-bands in the low frequency region and it is impossible to explore those relationships in low spectral resolution of BOLD acquired with typical parameters. This problem is further confounded by the long repetition time (TR) used for these experiments, which results in aliasing of harmonics of physiological rhythms into lower frequency components.

Functional Connectivity in Animal Models

To better understand the relationship between neural activity and functional connectivity, several groups have recently turned to animal models. Functional networks similar to those observed in humans have been observed in monkeys and rats using fcMRI. The use of animal models allows for more invasive experimental designs which can give deeper insight into the LFFs. Also, more controlled experiments are possible when animal models are used. Since animals are kept under the same conditions and are anesthetized during the experiments, inter-subject differences are minimized. The presence of coherent low frequency BOLD fluctuations has been demonstrated in

somatosensory and visual networks in anesthetized rats and monkeys (Williams, Peltier et al. 2006; Vincent, Patel et al. 2007; Pawela, Biswal et al. 2008). Additionally, the default mode network has been shown to exist in anesthetized monkeys using fcMRI (Vincent, Patel et al. 2007). These findings justify the use of these animal models in studies to better explore the basis of functional connectivity. Some of these studies have provided additional evidence of a link between coordinated neural activity and functional connectivity. Anesthesia-dependent changes in delta power correlation were shown to co-vary with changes in functional connectivity in rats, although the measurements were not performed simultaneously due to technical limitations (Lu, Zuo et al. 2007). Shmuel and Leopold reported correlations between the band-limited power of gamma rhythm in spontaneous neural activity and BOLD fluctuations in the visual cortex of monkeys in the absence of any stimulus (Shmuel and Leopold 2008). These results are an extension of previous work showing very slow (< 0.1 Hz) coherent oscillations in the band limited power of local field potentials obtained from monkey visual cortex (Leopold, Murayama et al. 2003). The envelope of the EEG (f < 30Hz) has also been shown to predict fluctuations in cerebral blood flow measured using laser Doppler flowmetry in rats (Liu, Zhu et al. 2008). A more recent study suggests that the spontaneous fluctuations in the LFPs (especially 40-80 Hz range) measured from a single cortical site in monkeys at rest exhibit widespread, positive correlations with fMRI signals over nearly the entire cerebral cortex (Schölvinck, Maier et al. 2010).

To sum up, LFFs and functional connectivity can be observed in the animal models even in the anesthetized state. Invasive multimodality studies performed on the animal models shows link between the LFFs in BOLD and electrical activity of the brain.

The use of animal models can help us overcome the limitations of human studies and therefore provides an attractive alternative for studying properties and significance of LFFs and functional connectivity.

Spatiotemporal Dynamics of LFFs

As stated above, current techniques focus on detecting correlations among different brain regions that are assumed to persist over several minutes (Biswal, Yetkin et al. 1995; Cordes, Haughton et al. 2002; van de Ven, Formisano et al. 2004). However, EEG and magnetoencephalography (MEG) studies indicate that transient coordination of brain areas occurs on time scales ranging from milliseconds to tens of seconds (de Pasquale, Della Penna et al. 2010). Since BOLD signal is correlated with neural activity, it is possible that such time-varying features might exist in fMRI data as well.

In a recent study using high temporal resolution data obtained from rats, we demonstrated that frame-by-frame visualization of band-pass filtered BOLD time-courses exhibits discrete spatiotemporal events, suggesting that detection of individual events in the data is possible (Majeed, Magnuson et al. 2009). Waves of high signal intensity propagating from secondary somatosensory cortex (SII) to medial cortical areas were observed in α-chloralose anesthetized rats. These areas are not part of the same network when traditional seed-based cross-correlation techniques are used, indicating that the conventional methods may not extract all the information that can be obtained from functional connectivity data (Williams, Magnuson et al. in press). This opens a new avenue for functional connectivity research. The detection of propagating waves of MRI signal fluctuations that may reflect slow changes in electrical activity naturally leads to

speculation about whether other dynamic neural events can be detected with MRI in anesthetized rodents, and whether similar spatiotemporal patterns / events can be found in awake humans. In support of that idea, a recent study reports variability in the coherence between posterior cingulate cortex and task-positive network over time (Chang and Glover 2009). These studies highlight the need for novel analysis techniques that could capture time-varying features in spontaneous BOLD fluctuations.

An in-depth study of the spatiotemporal patterns in fcMRI data may help to elucidate the origin and significance of LFFs. For example, it has been proposed that LFFs in different brain regions may be caused by one or more subcortical sources or "drivers" (Drew, Duyn et al. 2008). Identification of sources of the high intensity signal can identify possible drivers / regions receiving direct input from the drivers of the LFFs in BOLD. Also, if similar spatiotemporal patterns can be detected in humans, it may be possible to tie these events to behavioral performance data.

Our preliminary exploration of the spatiotemporal patterns of spontaneous BOLD fluctuations was based purely on visual inspection (Majeed, Magnuson et al. 2009). The amplitude of the low frequency BOLD fluctuations is small, typically ~1-2%, and visual detection of the patterns is limited by signal to noise ratio (SNR), and thus it is possible that patterns may be obscured in the presence of noise. Therefore, it is desirable to have an automatic method for the detection of such patterns. The previous study examined only single slice data, so that analysis was restricted to a single coronal plane. Three-dimensional data is necessary to characterize the true direction of propagation, which may contain significant through-plane components.

Research presented in this document provides a framework for detecting and analyzing dynamic events in BOLD data in absence of any external stimulation. First, the presence of visually detectable spatiotemporal patterns in rat data is demonstrated. Further, an automatic spatiotemporal pattern detection algorithm is developed and characterized. The algorithm is applied on human and rat data for detecting multiple reproducible spatiotemporal patterns. Finally, a method for estimating the contribution of the patterns towards LFFs is proposed and applied to human and rat data. This research opens a new avenue for the functional connectivity research and is likely to have significant impact on interpretation of functional connectivity and LFFs.

CHAPTER 2

VISUAL DETECTION OF SPATIOTEMPORAL PATTERNS IN RATS

In this chapter, the presence of visually detectable spatiotemporal patterns in BOLD fluctuations in rats is demonstrated. Most groups utilize TRs that are not short enough for separation of respiratory and cardiac cycles in the frequency domain (Lu, Zuo et al. 2007; Pawela, Biswal et al. 2008; Zhao, Zhao et al. 2008). Also, longer TRs are likely to limit our ability to resolve the dynamic patterns. We describe the acquisition of functional connectivity data from the rat with high temporal resolution that allows separation of the primary cardiac and respiratory components from the frequencies of interest and allows the identification of two low frequency peaks in the data acquired from the rat cortex. The low frequency peaks exhibit different functional connectivity specificity, suggesting that they might represent different neural/vascular processes. We further characterize spatiotemporal characteristics of both peaks and identify patterns of LFF propagation which may not be deduced from typical functional connectivity analysis methods.

Materials and Methods

Animal Preparation

For this study, all experiments were performed in compliance with guidelines set by the National Institutes of Neurological Disorders and Stroke ACUC. Six adult male Sprague-Dawley rats (168–234 g) were initially anesthetized with 5% halothane and

maintained at 1.5% halothane during the following surgical procedures. Each rat was orally intubated and placed on a mechanical ventilator throughout the surgery and the experiment. Plastic catheters were inserted into the right femoral artery and vein to allow monitoring of arterial blood gases and administration of drugs. Two needle electrodes were inserted just under the skin of each forepaw, one between digits 1 and 2, and the other between digits 3 and 4. After surgery, the rat was given an i.v. bolus of α-chloralose (80 mg/kg) and halothane was discontinued. Anesthesia was maintained with a constant α-chloralose infusion (27 mg/kg/hr) (Silva, Lee et al. 1999; Keilholz, Silva et al. 2004).

The rat was placed on a heated water pad to maintain rectal temperature at ~37°C while in the magnet. Each animal was secured in a head holder with ear bars and a bite bar to prevent head motion and was strapped to a plastic cradle. End-tidal CO_2, rectal temperature, tidal pressure of ventilation, heart rate, and arterial blood pressure were continuously monitored during the experiment. Arterial blood gas levels were checked periodically and corrections were made by adjusting respiratory volume or administering sodium bicarbonate to maintain normal levels when required. An i.v. injection of pancuronium bromide (4 mg/kg) was given once per hour to prevent motion.

One of the rats was euthanized at the conclusion of the experiment without being removed from the scanner and an additional series of BOLD-weighted images was acquired to serve as a control dataset.

MRI

All images were acquired with an 11.7 T / 31 cm horizontal bore magnet (Magnex, Abingdon, UK), interfaced to an AVANCE console (Bruker, Billerica, MA) and equipped with a 9-cm gradient set, capable of providing 30 G/cm with a rise time of

65 μs. Shimming was performed with a custom-built shim set and high power shim supply (Resonance Research, Billerica, MA). A contoured rectangular surface coil (2 x 3 cm) that attached to the head holder was used to transmit and receive the MR signal. Scout images were acquired in three planes with a fast spin echo sequence to determine appropriate positioning for the functional Study. A spin-echo, EPI sequence was used to acquire a series of images during forepaw stimulation (2 mA current, 300 μs pulses repeated at 3 Hz) in order to locate the slice containing primary somatosensory cortex (SI). Setup included shimming, adjustments to echo spacing and symmetry, and B0 compensation. A single-shot sequence with a 64×64 matrix was run with the following parameters: effective echo time 30 ms, repetition time 1.0–1.5 sec, bandwidth 200 kHz, field of view 1.92×1.92 cm. Whole-brain coverage was obtained with 10–11 2-mm thick slices, spaced 0.2 mm apart.   The paradigm consisted of 60 images during rest, followed by 30 images during forepaw stimulation, and another 60 images during rest. Functional connectivity data were acquired with gradient echo EPI on the slice containing SI with following parameters: repetition time 100 ms, echo time 20 ms (15 ms for one rat), field of view 1.92×1.92 cm, 2mm thick slice, 3600 repetitions. No stimulation was given during these scans.

Preprocessing

The area comprising the brain was segmented using an intensity threshold and manual removal of remaining voxels outside the brain. The datasets were spatially blurred using a 3×3 Gaussian filter with $\sigma = 2$ pixels All analysis was performed using Matlab (MathWorks, Natick, MA) unless otherwise noted. The first 500 time-points were discarded before power spectral analysis and after all the filtering operations

described later in order to discard transient effects of data acquisition and filtering. Resultant time-courses were de-meaned and quadratic detrending was performed.

Power Spectral Analysis

Power spectra were obtained for time-courses from SI and secondary somatosensory cortex (SII) using the Welch method (8 sections with 50% overlap, Hamming window). Visual inspection suggested the presence of two low frequency peaks, LF1 ($f < 0.05Hz$) and LF2 ($0.11Hz < f < 0.18Hz$), in three of the datasets obtained from live rats (described later in results). Only the lower peak (LF1) was visually detectable for the other three datasets from live rats. Peaks due to respiration and cardiac noise were also observed. Frequencies of respiratory and cardiac contributions were assessed by inspecting the spectra of the signals from the brain regions near the draining veins, including sagittal sinus and the surface of the cortex. No specific peaks were observed for dead rat.

Spatial Localization of Spectral Peaks

Maps were created in order to assess the spatial localization of physiological noise and the low frequency peaks. We visually examined the spectra of time-courses obtained from different locations in the brain for LF1, LF2 (for the datasets showing LF2), cardiac and respiratory peaks, and noted the frequencies of the corresponding peaks for each dataset. Band-pass or low-pass filtering (3rd order Butterworth filter) was used to isolate the time-courses corresponding to the individual peaks. The filtered time-courses were normalized to obtain percentage difference from mean signal intensity of the raw data. Maps showing the standard deviation of each contribution were obtained, reflecting spatial localization of contribution due to different peaks. Parameters used for one of the

16

live rats (rat 1) were used for processing the data from the dead rat since no visible peaks were present. Frequency cutoffs of 0-0.05 and 0.08-0.2 Hz were used for LF1 and LF2 respectively. Filters for physiological noise had their pass bands centered at respective frequencies, with a 3db width of 0.2 Hz.

Functional Connectivity Analysis

Six functional connectivity maps were obtained from each dataset using two different filters (0-0.05 Hz and 0.08-0.2 Hz) and three different seed locations (SI and SII and caudate-putamen (CP)). The seeds' time-courses were obtained by averaging filtered time-courses from a 3×3 manually chosen region in the areas of interest. Cross correlation between the seed time-course and time-courses from all the voxels in the brain was calculated to obtain correlation maps. To estimate localization of connectivity, the number of voxels passing an arbitrary cross-correlation threshold of 0.5 was calculated for bilateral regions of interest (ROIs) covering SI, SII and CP for each seed location. In addition, average time-courses were obtained for the ROIs defined on left and right SI, SII and CP and 6×6 correlation matrix was obtained.

Spatiotemporal Dynamics

Image-by-image visualization was used as a primary tool to study spatiotemporal dynamics. The preprocessed data was filtered and resulting time-courses were normalized individually to unit variance. The resulting data was displayed as a movie for visual detection of any spatiotemporal patterns. Using different filters, we were able to observe dynamics of LF1, LF2 and physiological contributions. The filters specifications were same as described above.
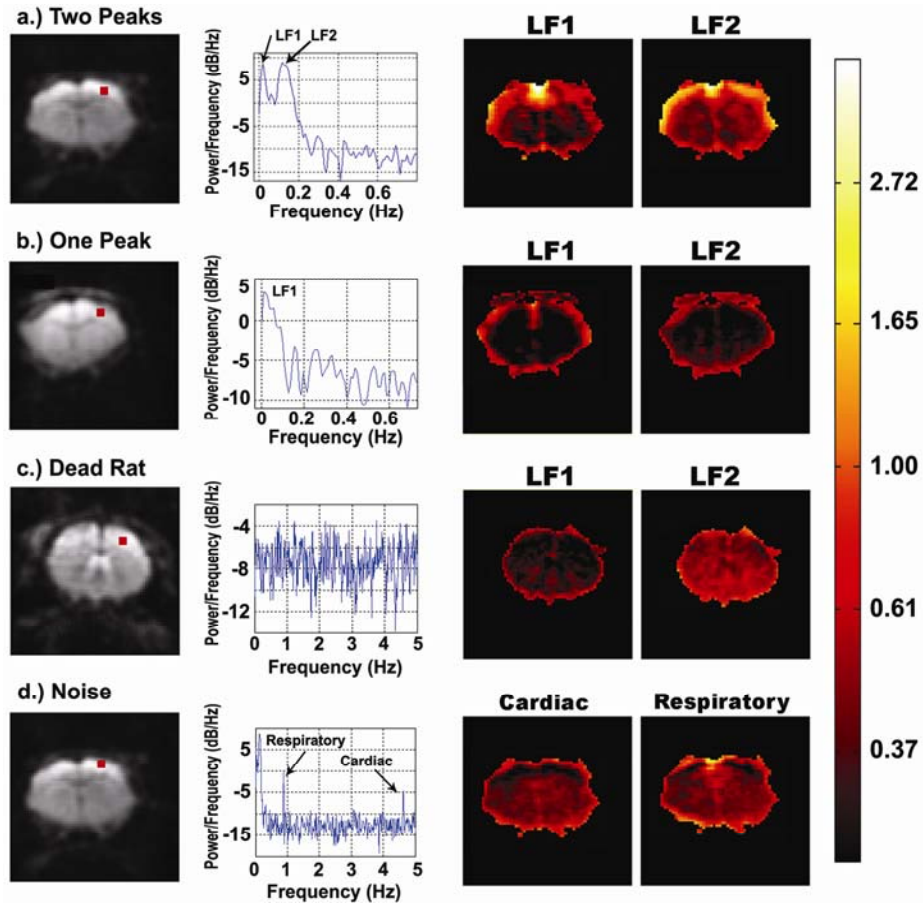
Figure 1: Location of seed on EPI image, power spectra of the signal obtained from seed location (with time-course normalized to unit variance), and band-limited maps of temporal standard deviation for a rat with two clear low frequency peaks (a), a rat with a single low frequency peak (b), a dead rat (c), and a rat that exhibited significant cardiac and respiratory signal (d). a) Power spectrum for a cortical seed ROI shows two distinct peaks for this rat. Spatial maps for LF1 (column 3) and LF2 (column 4) contributions demonstrate high cortical specificity for both peaks, with highest signal magnitude near the sagittal sinus for LF1. b) Power spectrum from another rat exhibits only one clear peak (LF1). The peak map for LF1 contribution (column 3) shows high specificity to cortex, again with a focal increase in power near the sagittal sinus. The power in the LF2 range is much lower and primarily confined to the surface of the brain. c) Power spectrum from a dead rat showing no clear peaks. 0-0.05 Hz (column 3) and 0.08-0.2 Hz (column 4) contributions are non-specific. d) Power spectrum from a cortical seed placed near the draining veins exhibits respiratory and cardiac contributions. Spatial distribution map for cardiac contribution (column 3) shows high specificity to the area near draining veins, whereas respiratory contribution (column 4) is strongest around the sagittal sinus, draining veins and ventricles.

Results

Power Spectral Analysis

Power spectral analysis of time-series obtained from cortical areas including SI and SII revealed two distinct low frequency peaks in the following frequency ranges for three rats: below 0.05 Hz (LF1), and between 0.11 and 0.18 Hz (LF2) (Figure 1a, column 2). Only a single peak was observed in the remaining three datasets, with the most of the power in the LF1 range (Figure 1b, column 2). Peaks corresponding to respiratory and cardiac noise were also observed (Figure 1d, column 2). The peaks detected at ~1 Hz and ~4.5 Hz were attributed to respiratory and cardiac cycles respectively, based upon the frequencies of the cycles monitored during the experiment (breathing rate: ~60 breaths/minute, cardiac rate: ~250 beats/minute). No obvious peaks were observed in the data obtained from the dead rat (Figure 1c, column 2).

Spatial Specificity of the Peaks

Figure 1a (columns 3 and 4) shows standard deviation maps for low frequency contributions for one of the datasets showing the two low frequency peaks. The LF2 appears with high magnitude in the cortex with high specificity, as apparent from the standard deviation map. LF1 contribution is also high in the cortex compared with the subcortex. Figure 1b (columns 3 and 4) shows the maps for a dataset without a clear LF2 peak. The LF1 maps are similar to those seen in rats with two peaks. In contrast, the LF2 no longer appears in the cortex with high magnitude compared with the subcortex. Peak distribution for the dead rat does not show any specific patterns (Figure 1c). The strongest respiratory contribution was observed primarily near the sagittal sinus, large blood vessels, and ventricles. The contribution from the primary cardiac peak was high

19

near large veins for most rats and occasionally also near the sagittal sinus. Examples from one rat are shown in Figure 1d. Edges and areas with low coil sensitivity appear with high magnitude in many of the standard deviation images, which may be expected because percentage difference due to noise factors will be large in those areas due to low baseline intensity.

Cross Correlation Analysis

The low pass (0-0.05 Hz) filter retained the LF1 peak, whereas the band pass (0.08-0.2 Hz) filter retained LF2. Figure 2 shows connectivity maps for a dataset with two peaks and a dataset with one peak, each with two different seed locations (SI and SII). The correlation maps for LF1 exhibit low sensitivity to the location of cortical seed regions and high correlation (> 0.5) is seen for the whole cortex and some sub-cortical areas. We observed this trend for LF1 for most seeds within cortex in all the datasets. In the datasets with two peaks, correlation maps based on LF2 exhibit higher specificity than the maps based on LF1. High correlation values are found primarily in the contralateral analogue of the seed region for a seeds placed in SI, rather than evenly distributed throughout the cortex. Some bilateral correlation for LF2 is also observed in the datasets with one peak (Figure 2b and Figure 3a). The average correlation value in the contralateral SI is greater than 0.4 for seeds placed in SI for maps created based on both LF1 and LF2 in datasets with both peaks (Figure 3a, rats 1-3). As expected, in rats with only the lower peak, correlation is reduced for LF2 (Figure 3a, rats 4-6). Figure 3b shows the average cross-correlation coefficients between all ROIs for LF1 and LF2. LF2 generally exhibits lower cross-correlation values, and strong correlation is mostly confined to bilateral cortical areas.
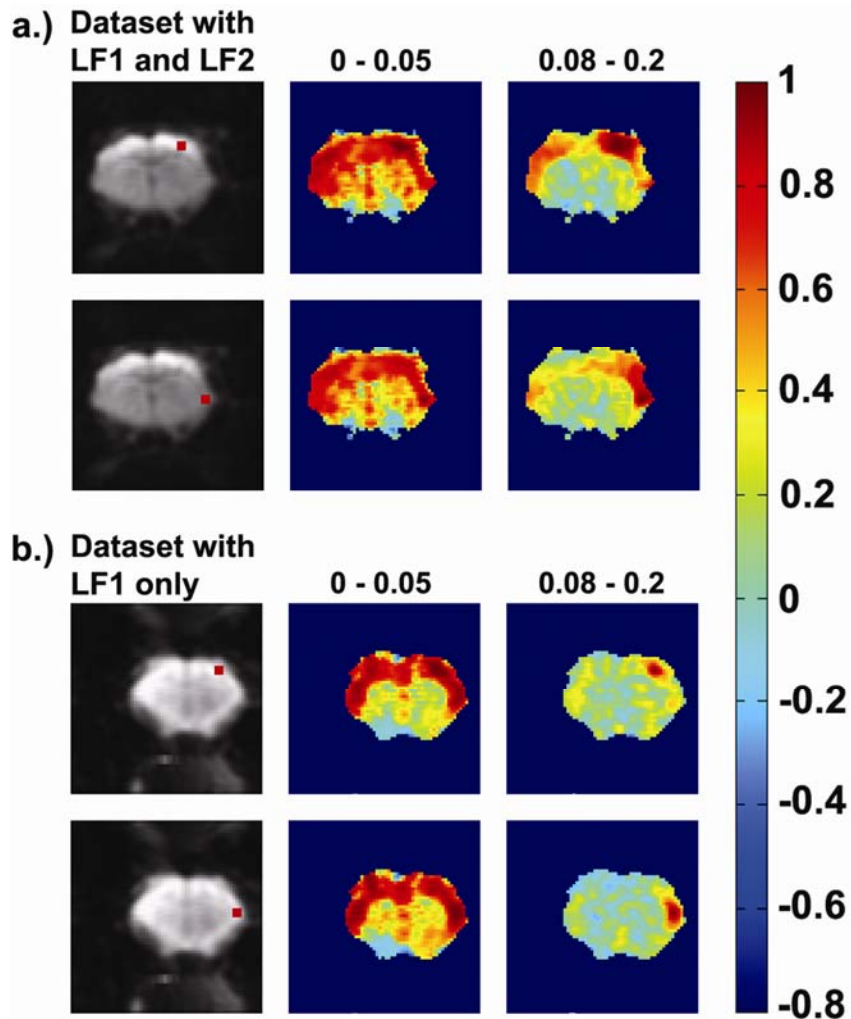
Figure 2: Connectivity maps created using time-courses filtered to retain LF1 (middle column) or LF2 (right column). The left column shows EPI images overlaid with seed ROIs. a) Connectivity maps from a rat with two well-defined spectral peaks. The seed locations are SI (first row) and SII (second row). Stronger correlation and less specificity is observed for LF1 compared with LF2. The correlation maps are less dependent upon the seed location for LF1. b) Connectivity maps from a rat with a single spectral peak. LF1 connectivity maps show strong correlation throughout the cortex that is relatively insensitive to the location of the seed, similar to a. The LF2 peak is more specific but less bilateral connectivity is observed than for the dataset with two peaks.
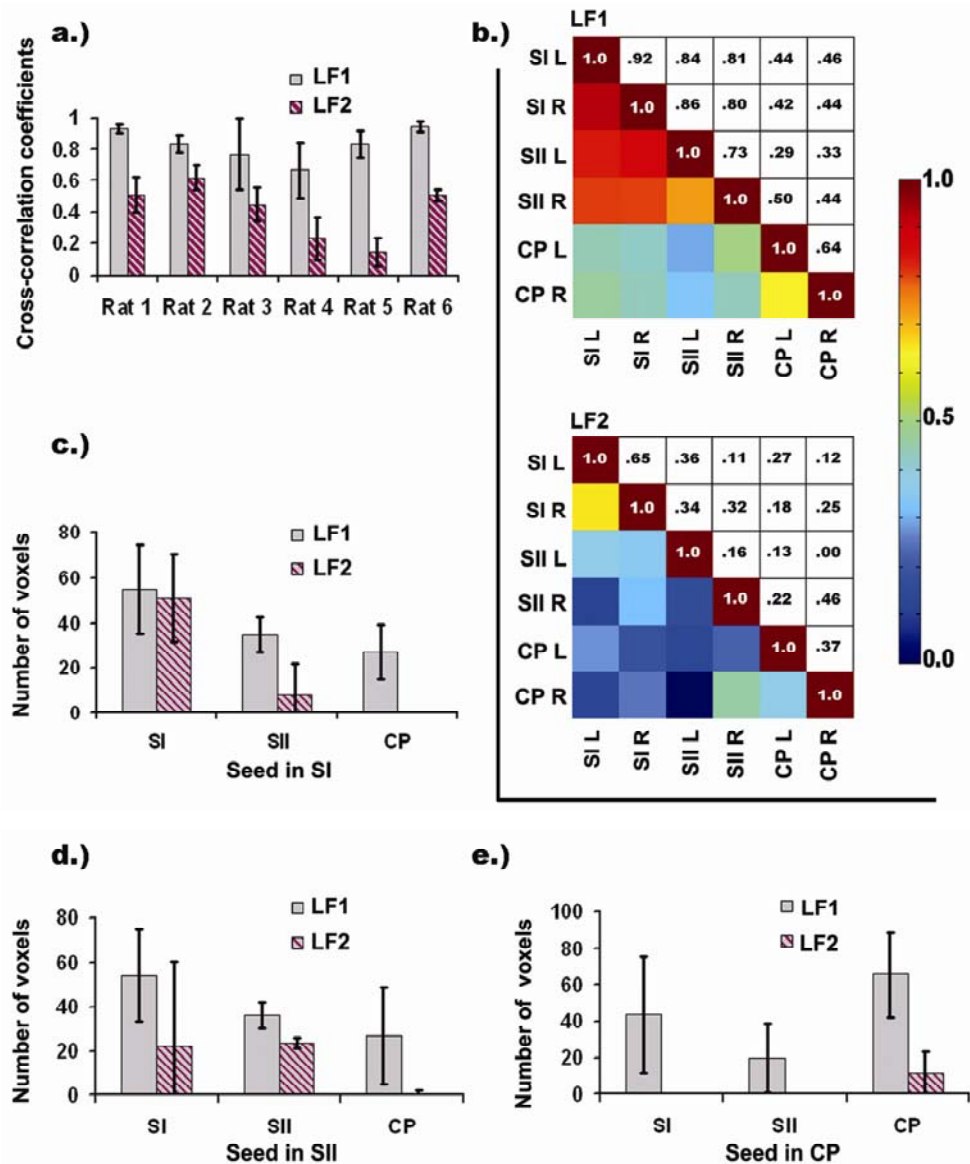
Figure 3: a) Average correlation in the region of interest (ROI) defined in the contralateral SI for a seed placed in SI: Rats 1-3 showed two clear peaks. Stronger correlation is observed for LF1 for all the datasets. b) Correlation matrix for average time-courses for different lcoations:Overall, stronger correlation is observed for LF1 c) and d) Number of voxels with correlation coefficient > 0.5 for seeds placed in SI and SII: Pixels crossing the threshold are restricted to the somatosensory cortex for LF2, whereas pixels crossing the threshold are distributed between SI, SII and CP for LF1. Also, the extent of the correlation in cortex and CP does not vary with the cortical seed location for LF1 (maximum difference < 2 voxels for seeds placed in SI and SII) e) Number of voxels with correlation coefficient > 0.5 for seed placed CP: No pixels in SI and SII show correlation > 0.5 for LF2, whereas the pixels crossing the threshold are distributed between SI, SII and CP for LF1

Please note that only three datasets showing the two peaks were used for the results shown in figure 3. Inclusion of the remaining 3 datasets yields qualitatively similar results.

To better quantify the specificity of each peak, the number of voxels with cross-correlation values of greater than 0.5 were measured in anatomically drawn ROIs in SI, SII, and CP. Figure 3c-d shows that LF1 maps are relatively independent of cortical seed location, as compared with LF2. The average number of voxels with cross correlation greater than 0.5 in different regions shows much smaller variability for LF1 compared with LF2 for seeds placed in SI and SII. The maximum difference between voxels crossing the threshold (0.5) for seeds placed in SI and SII is less than 2 voxels for LF1 and approximately 29 voxels for LF2. The high magnitude of error bars seen in Figure 3c-e is due to variability in the number of voxels in different areas across rats because of variation in slice orientation. Correlation values observed for LF1 were in general higher in comparison with those obtained for LF2 (Figure 3a-b).

As seen in Figure 3c and d, very few voxels in CP (less than 1, on average) have the LF2 cross correlation values above 0.5 for seeds placed in SI and SII. Also, no voxels in SI and SII showed LF2 correlation coefficient above 0.5 for seeds placed in CP. In contrast, correlation coefficients for both cortical and subcortical pixels crossed this threshold for the same seeds for LF1. These observations suggest that LF2 correlation maps are more specific to the networks in which the seed is placed, in agreement with previous work that identified separate, well-delineated networks in SI and CP (Zhao, Zhao et al. 2008)

Spatiotemporal Dynamics

Image by image visualization of LF2 signal (from the rats exhibiting two clear peaks) revealed consistent, well-organized spatiotemporal patterns. The most prominent pattern, that was observed in all the datasets, is displayed in Figure 4a-b. This pattern

looks like a propagating wave, with high signal intensities starting from SII and traveling

along the cortex. Intensity fluctuations were approximately 2-4%. The waves were

bilateral in most cases, but unilateral propagation was occasionally observed. The travel

time of the waves from SII to MI was consistent across rats, based upon visual inspection

(mean = 4.7s, standard deviation = 0.4, 0.9 and 0.8 respectively). The waves were not

uniformly distributed in time but tended to occur in clusters (Figure 5). No organized

patterns were seen when 0.08-0.2 Hz component was visualized in the same way for the

datasets with one peak only. The most prominent pattern for the LF1 signal, in contrast,

was a slow change in intensity throughout the whole brain, moving from the surface to

the center (Figure 4c). Movies that more clearly show these spatiotemporal dynamics for

two different rats are available online as supplementary material (Movies 1 and 2).

Application of the same method to the respiratory and cardiac signals revealed

different patterns, primarily involving large vessels and areas near the ventricles Figure

6a-b. No organized patterns were detectable in the datasets obtained from the dead rat

Figure 6c. Movies showing dynamics of respiratory and cardiac noise are available online

as supplementary material (Movies 3 and 4).
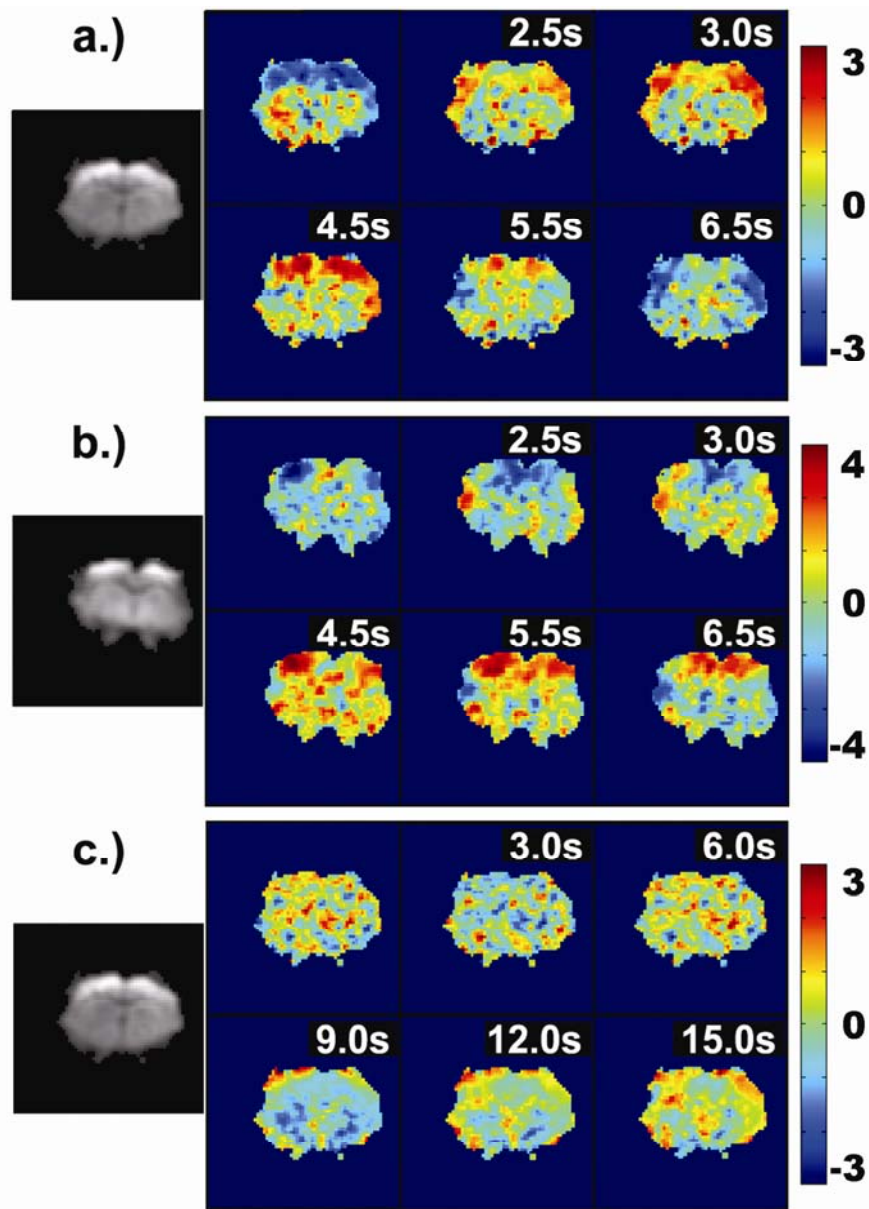
Figure 4: Spatiotemporal dynamics for LF2 and LF1 peaks. a) Propagating waves were observed in the datasets filtered to retain LF2. A bilateral wave of low signal intensity in SI moves medially as areas of high intensity arise in SII (2.5-3 s after the start of the sequence). The wave of high intensity moves medially and the cycle begins again with the appearance of bilateral areas of low intensity in SII (6.5 s). b) Waves observed in the LF2-filtered data in another rat. The pattern of propagation is similar to a. c) LF1 shows completely different propagation patterns. The most prominent pattern was a slow propagation of signal intensity from the surface of the brain inward. The pattern moves through layers and does not show functional specificity. No cortical waves similar to those shown in a and b were observed.
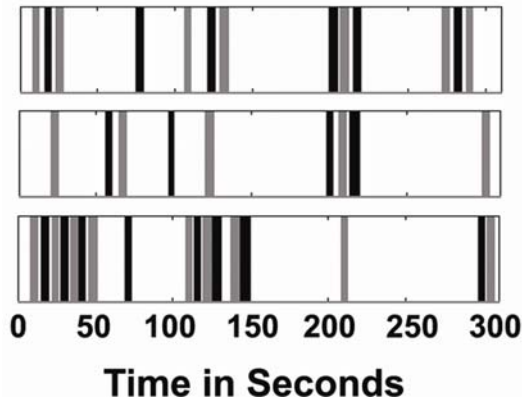
Figure 5: Temporal pattern of occurrence of the waves: Plot of the occurrence of waves (after filtering the data to retain LF2) for all three rats that exhibited a clear LF2 peak is shown. The waves appear to occur in groups. Alternate waves are colored differently in order to separate consecutive occurrences. The duration of the waves is defined as the time required for the high intensity to travel from SII to MI.

Summary and Discussion

Two low frequency peaks (LF1 and LF2) were detected in high spatial and temporal resolution rat data. The peaks exhibit different functional connectivity patterns and spatiotemporal characteristics. In this experiment, both the spectral resolution and the sampling rate were higher than in typical human studies, providing clear separation of the low frequency peaks and preventing aliasing of first harmonics of the cardiac or respiratory cycles.

It is interesting to note that LF2 is not observed as a well-separated peak in 3 of the datasets. However, some LF2 connectivity is also observed in the datasets with only one peak, suggesting presence of some LF2 signal (Figures 2 and 3). This weak presence might be reflected as broadening of the LF1 peak (Figure 1b). The short repetition time used in this study to avoid aliasing of the primary cardiac component results in a low signal-to-noise ratio, which may limit our ability to detect and separate the two peaks.

26

This study was also limited by the small number of animals (n=6), imaged on a different MRI system than the one currently in use.

The properties of spatiotemporal events observed in the data, when combined with multimodality data and information about different factors contributing to the BOLD signal, might provide clues to the origin of the LFFs. In addition, if and when neural origin of LFFs is confirmed, such techniques would provide us with a convenient and non-invasive method of probing the transient aspects of resting brain under normal and pathological conditions.
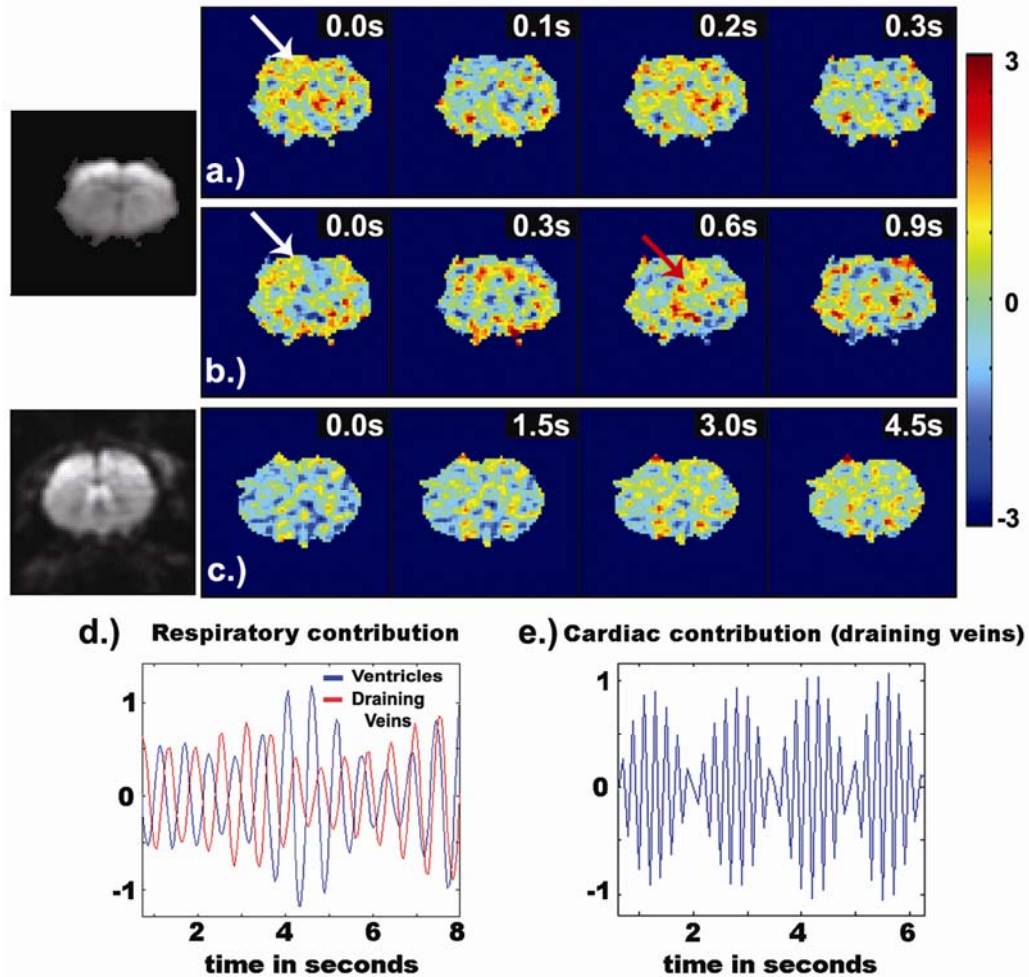
Figure 6: Spatiotemporal dynamics related to physiological or scanner noise. No patterns of cortical waves similar to those shown in 4a and b were observed. a) Contribution from the primary cardiac peak. The only clear pattern forms around the draining veins along the surface of the cortex (pointed by white arrow), which alternately brighten and darken. b) Contribution from the primary respiratory peak. Periodic changes in signal intensity are apparent in the draining veins along the surface (white arrow) and the areas near the ventricles (red arrow). Interestingly, these changes are out of phase. c) Contribution of LF2 frequency range in the dead rat. No specific patterns can be detected, indicating that scanner noise is not the source of the waves. d and e) Time courses for respiratory and cardiac contributions. Respiratory contributions from ventricles and draining veins have different phases. The time-courses were normalized to unit variance before plotting.

CHAPTER 3

AUTOMATIC DETECTION OF SPATIOTEMPORAL PATTERNS

Our preliminary exploration of the spatiotemporal patterns of spontaneous BOLD fluctuations was based purely on visual inspection (Chapter 2). The amplitude of the low frequency BOLD fluctuations is small, typically ~1-2%, and visual detection of the patterns is limited by signal to noise ratio (SNR), and thus it is possible that patterns may be obscured in the presence of noise. A novel approach for detection of repeated spatiotemporal patterns is presented in this chapter.

Preprocessing

The data is preprocessed prior to the application of the algorithm. The essential preprocessing steps include temporal filtering and normalization of each time-course to unit variance. Temporal filtering is necessary in order to increase the effective SNR by removing the frequency components that might not be of interest (e.g. respiratory and cardiac cycles) while retaining the LFFs. The time-courses are normalized to unit variance in order to make sure that no patterns are left undetected merely due to low amplitude of the fluctuations in a given area. As a side effect of normalization to unit variance, intrinsic weighting of the results towards the areas comprising fluctuations with high variance is no longer preserved.. Other preprocessing steps (spatial blurring, and spatial normalization to a standard image space and removal of nuisance signals including motion parameters and signals from whole brain, white matter and CSF) may also be applied, but are not necessary.

The Algorithm

To improve on the original approach of visual inspection described in Chapter 2, an algorithm was developed to identify recurring spatiotemporal patterns in the data without user input, using a random starting location and an iterative, correlation-based approach (Figure 7). A template, consisting of several consecutive preprocessed images is created with a random starting image (Figure 7a). Sliding correlation of the template with the preprocessed image series is obtained in order to locate the segments of images in the image series that are similar to the template (Figure 7b-c). The segments are averaged to obtain a new template (Figure 7d) and the process is repeated until the further iterations do not result in any modification in the template. If a spatiotemporal pattern occurs repeatedly and is captured by the initial template, it is possible to obtain high SNR approximation of the pattern using this approach. The detailed description of the algorithm is given below (summarized in Figure 7):

1. An initial guess about the duration of spatiotemporal patterns to be detected is chosen, termed window length (WL). WL can be based upon the duration of events observed visually. For example, the initial WL for the rats was chosen based on the duration of the patterns seen in our previous work presented in Chapter 2, also reported in (Majeed, Magnuson et al. 2009). Alternatively, different experimental values of WL can be used in order to explore spatiotemporal events with different time scales in the data.
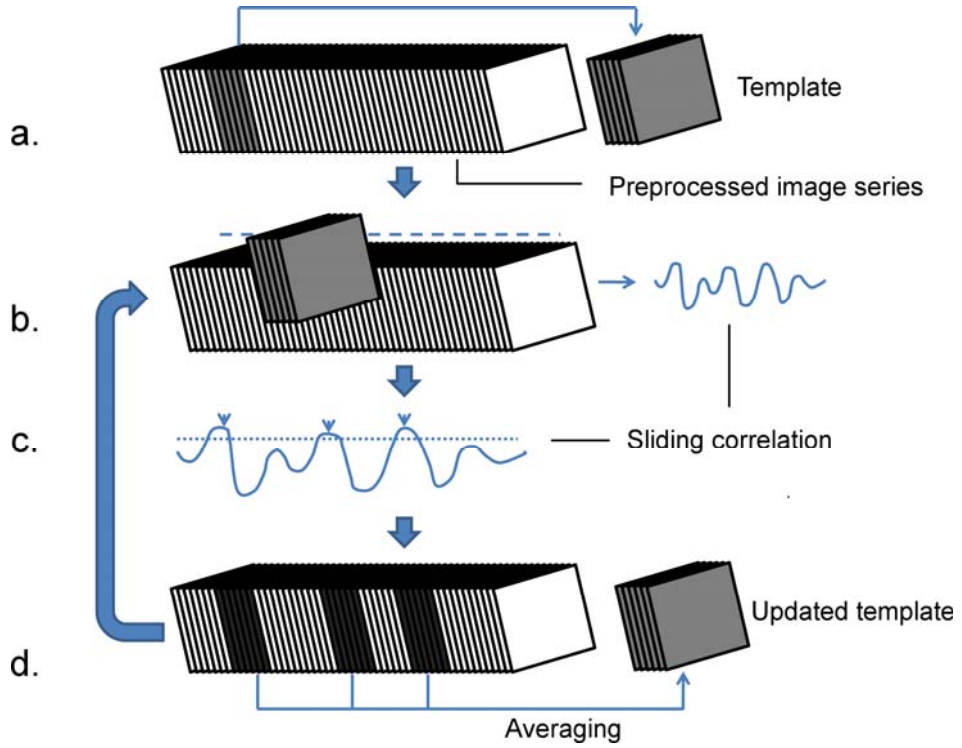
Figure 7: Algorithm for automatic detection of dynamic patterns. a) A chunk of consecutive images starting at a random time is selected from the filtered image series to serve as template. b) Sliding correlation between the filtered image series and the template is obtained. c) Peaks are detected in the thresholded sliding correlation. d) Chunks of images corresponding to the peaks correlation values are averaged in order to obtain updated template. Steps b to d are repeated until the template does not change for two successive iterations (cc > 0.9999).

2. A random image in the preprocessed image series is chosen as a starting point for the template time-series (Figure 7a). The time location corresponding to the starting point is termed q and referred to as the "seed time-point" later in the text. A template is essentially a series of consecutive images, with its duration equal to WL

.

$$T(x, y, z, n) = I(x, y, z, n + q - 1) \qquad 1 \le n \le WL$$

3. Sliding correlation $r(n)$ between the preprocessed image series $I(x, y, z, k)$ and template $T(x, y, z, k)$ is obtained (Figure 7b) using following equation (N_s represents number of voxels in the ROI):

31

$$r(n) = \frac{1}{K(n)} \sum_{m=n}^{n+WL-1} \sum_{(x,y,z)\in s} \big(I(x,y,z,m) - \mu_I(n)\big)\big(T(x,y,z,m-n+1) - \mu_T\big)$$

where

$$\mu_T = \frac{1}{(N_s.WL)} \sum_{m=1}^{WL} \sum_{(x,y,z)\in S} T(x,y,z,m), \quad \mu_I(n) = \frac{1}{(N_S.WL)} \sum_{m=n}^{n+WL-1} \sum_{(x,y,z)\in S} I(x,y,z,m)$$

$$K(n) = \sqrt{\sum_{m=1}^{WL} \sum_{(x,y,z)\in S} \big(T(x,y,z,m) - \mu_T\big)^2} \sqrt{\sum_{m=n}^{n+WL-1} \sum_{(x,y,z)\in S} \big(I(x,y,z,m) - \mu_I(n)\big)^2}$$

$r(n)$ represents sliding correlation at temporal delay equal to n images. S is the set of spatial coordinates (x, y, z) belonging to the region of interest (ROI) chosen for spatiotemporal analysis. $I(x, y, z, k)$ and $T(x, y, z, k)$ represent intensity values of the preprocessed image series and template respectively at spatial location (x, y, z) in the kth image of the corresponding image series.

4. Time values corresponding to local maxima of $r(n)$ are obtained (Figure 7c). An array v with length p consisting of time-values for which local maxima are greater than a correlation threshold, is created.

5. The template is updated by averaging the segments of images corresponding to local maxima, using the following expression (Figure 7d):

$$T(x,y,z,n) = \frac{1}{p} \sum_{m=1}^{p} I(x,y,z,v(m)+n-1) \qquad 1 \le n \le WL$$

6. Steps 1-5 are repeated until $r(n)$ does not change for two successive iterations (cc (correlation coefficient) > 0.9999).

The value of correlation threshold can be modified during the iterations. For this study, lower threshold value (0.1) was chosen for the initial 3 steps, followed by higher value (0.2) for the subsequent steps.

The final template obtained after convergence is used as the representative spatiotemporal pattern, and peaks in the thresholded final sliding correlation time-course indicate occurrence times for the pattern. After the convergent correlation time-course is obtained, templates with expanded window length (WL') can be obtained by averaging the segments of images centered on the peaks in the thresholded correlation time-course in order to visualize any significant averaging outside the window chosen for the analysis. Although the voxels outside the ROI are not used for calculating and optimizing the sliding correlation, the final template can be obtained by including the whole image in the final averaging process (Figure 7d).

Validation of the Algorithm

In this section, the algorithm is validated by applying it to 1) data containing visually detectable propagating waves, as described in Chapter 2; 2) data from a dead rat. It is demonstrated that the algorithm detects the pattern that can be visually observed in the data. Further, no functionally specific pattern is observed for data obtained from a dead rat.

Application on Data with a Known Pattern

As shown in Chapter 2, propagating waves can be visually observed from lateral-medial direction in the rat cortex. The algorithm for pattern detection was applied to the same data (100ms TR, 20ms TR, 3600 repetitions, 0.08-0.2 Hz filter) in order to see if the visually observable pattern could be detected using the automatic detection algorithm (ROI placed in the cortex). Figure 8 shows eight frames from the template obtained from one of the rats (window length = 9s). This demonstrates that the visually observable lateral to medial propagation of intensity can be detected using the algorithm. The same

pattern was detected for all the rats, based upon visual inspection of the templates. Propagation of intensity from lateral to medial areas of the cortex was used as the criterion for detecting presence of the pattern.

Application on Data from a Dead Rat

The method was applied on the data obtained from a dead rat (100ms TR, 20ms TR, 3600 repetitions). As expected, the detected pattern did not show any functional specificity and consisted of global changes in intensity (Figure 9).
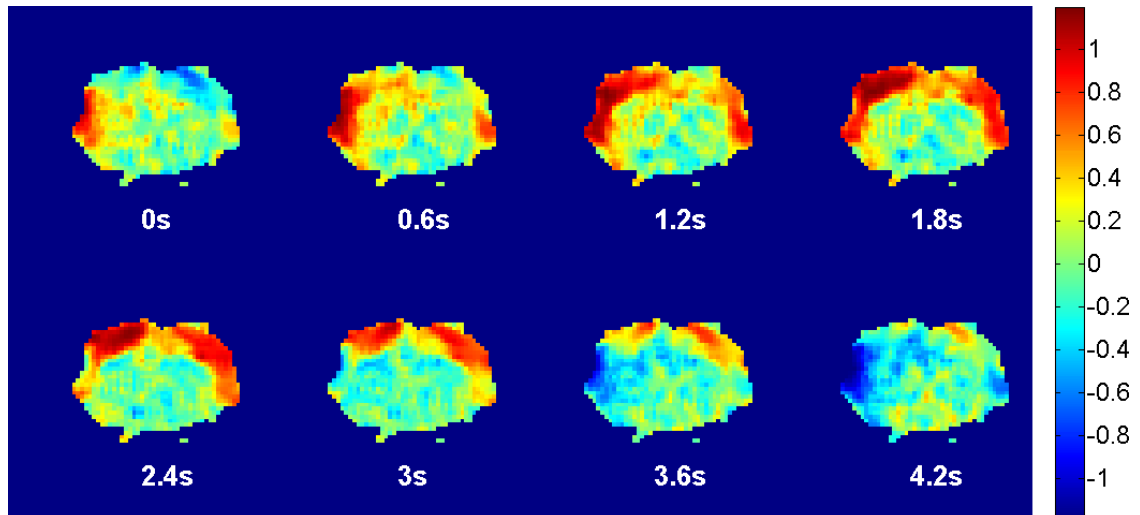
Figure 8: Automatically detected spatiotemporal pattern for an α-chloralose anesthetized rat. The figure shows eight frames from the final template obtained using the algorithm for detection of spatiotemporal patterns. Consistent with visually detected pattern reported in the Chapter 2, a wave of high intensity originates in SII (0s) and propagates in medial direction.
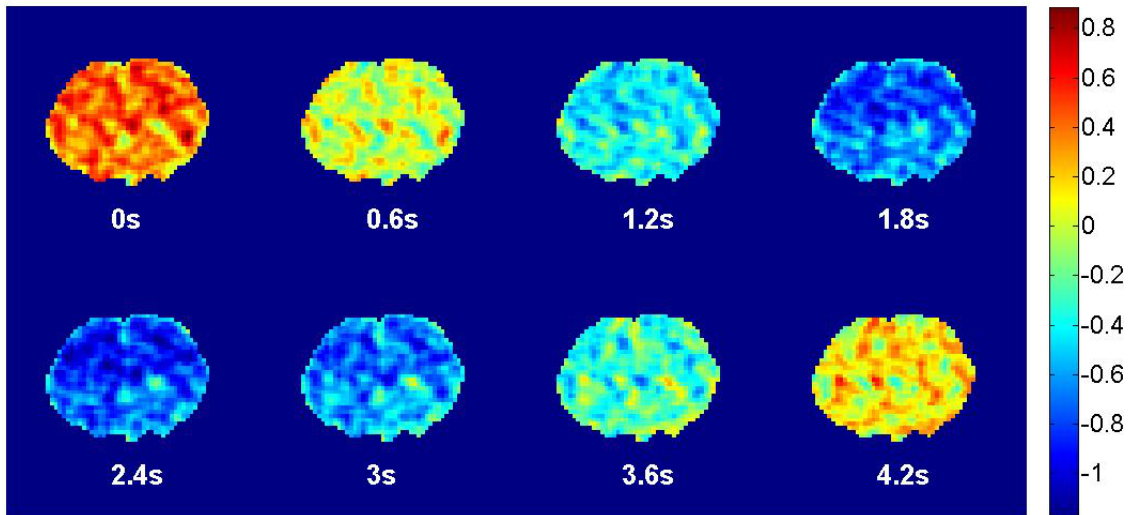
Figure 9: Automatically detected spatiotemporal pattern for a dead rat. As expected, the pattern detected in the data obtained from a dead is not functionally specific and consists of global changes in intensity.

Summary and Discussion

In this chapter, a novel pattern finding algorithm is presented for detecting spatiotemporal patterns in spontaneous BOLD fluctuations. The method generates a high SNR approximation of the pattern captured by initial template (a chunk of images starting at a random time) by finding its matches throughout the image series and averaging them. As reported in Chapter 2, visually detectable propagating waves were observed in filtered and normalized data obtained from α-chloralose anesthetized rats. The automatic detection algorithm successfully detected the visually observable pattern, demonstrating that the method is sensitive to the patterns present in the data, and the final template provides a faithful representation of the original pattern present in the data. Additionally, no specific patterns were detected in the data obtained from the dead rat, which suggests that the propagation pattern detected by the method may not be attributed to the scanner noise. The lateral to medial propagation was visually detectable only in 3 out of 6

35

datasets presented in Chapter 2. LF2 did not appear as a distinct peak in the 3 rats which did not show the propagation pattern. We re-analyzed that data using the pattern detection approach used in this study (0.08-0.2 Hz filter) and were able to detect the propagation pattern in the three datasets for which the pattern was not visually detectable (Movie 5). This highlights the improved detection sensitivity achieved by this method, compared with visual detection and suggests the presence of some LF2 contribution in those 3 rats, even though LF2 peak was not clearly observed visually. Application of the algorithm on phase-randomized data did not result in any functionally specific patterns for all the rats.

As described earlier, the method utilizes two pre-defined parameters, namely window length and seed time-point. The effect of variation in those parameters is characterized separately for human and rat data in the later sections. Also, the ways in which the algorithm can be used for exploratory analysis are also discussed.

CHAPTER 4

AUTOMATIC DETECTION OF SPATIOTEMPORAL PATTERNS

IN MULTISLICE RAT DATA

The previous study examined only single slice data, so that analysis was restricted to a single coronal plane. Three-dimensional data is necessary to characterize the true direction of propagation, which may contain significant through-plane components. A TR of 100ms was used in the experiment described in Chapter 2. However, acquisition of multislice data requires more frequent switching of gradients between the repetitions, and therefore a longer TR is required in order to avoid gradient overheating. In this chapter, detection of spatiotemporal patterns in multislice rat data with 500 ms TR is described. Also, dependence of results on initial parameters (window length, seed time-point) is investigated to estimate the robustness of the method.

Materials and Methods

Animal Preparation

All experiments were performed in compliance with guidelines set by the Emory University Institutional Animal Care and Use Committee (IACUC). Eight rats were initially anesthetized with 5% isoflurane and maintained at 2% isoflurane during preparation for imaging. Two needle electrodes were inserted just under the skin of each forepaw, one between digits 1 and 2, and the other between digits 2 and 3. The rat was given a bolus of medetomidine (0.05 mg/kg) and isoflurane was discontinued. Anesthesia was maintained with a constant medetomidine infusion rate (0.1 mg/kg/hr). The rat was

placed on a heated water pad while in the magnet to maintain body temperature at 37º C. Each animal was secured in a head holder with ear bars and a bite bar to prevent head motion and was strapped to a plastic cradle. Heart rate and blood oxygen level were continuously monitored during the experiment.

Animal Imaging

All images were acquired with a 9.4T / 20 cm horizontal bore BRUKER magnet, interfaced to an AVANCE console (Bruker, Billerica, MA) and equipped with a gradient set capable of providing 20 G/cm with a rise time of 120 µs. A two-coil actively decoupled imaging setup was used (2 cm diameter surface coil for reception and 7 cm diameter volume coil for transmission; Bruker, Billerica, MA) to achieve maximal SNR over the cortical areas of interest. Scout images were acquired in three planes with a FLASH sequence to determine appropriate positioning for the fMRI study. A gradient-echo EPI sequence (64×64 matrix, echo time (TE) 15-20 ms, repetition time (TR) 1.5 sec, field of view 2.56 cm × 2.56 cm) was used to acquire a series of images during forepaw stimulation in order to locate the slice containing the forepaw region of the primary somatosensory cortex (SI). A block design stimulation paradigm was used, consisting of alternating rest and stimulation blocks (4 mA current, 300 µs pulses repeated at 9 Hz, 30 TRs on, 30 TRs off). The slice containing the forepaw region of SI was used as a reference for slice placement for functional connectivity scans. Functional connectivity data were acquired with gradient echo EPI with following parameters: TR 500 ms, TE 20 ms, field of view 1.92 cm × 1.92 cm or 2.56 cm × 2.56 cm, 4 slices with 2mm thickness, 1200 repetitions. No stimulation was given during functional connectivity scans.

Data Processing

Rat datasets were analyzed separately for each subject. Preprocessing steps included motion correction, temporal filtering (0.08-0.2 Hz), spatial blurring and quadratic detrending. The algorithm described in Chapter 3 was applied on each dataset with manually chosen ROIs placed in 1) entire brain, 2) entire cortex, and 3) caudate-putamen (CP). Group analysis was not performed because inter-subject registration was not possible due to limited number of slices. Therefore, qualitative comparison was used for assessing reproducibility across the subjects. Consistency of some timing parameters (described later) was also evaluated in order to assess the reproducibility..

In order to test sensitivity of the algorithm on the pre-defined parameters, the algorithm was repeated with 1) different values of window length (WL) and 2) different values of seed-time point q. The results with different initial parameters were compared. In order to compare the templates, sliding correlation was obtained between the templates (WL' = 3WL, maximum lag = WL) and the maximum value of the sliding correlation was used as the similarity measure between the templates (termed as optimal correlation). Sliding correlation time-courses were compared using the same approach. In addition, the method was applied on phase-randomized data from a living rat. The phase-randomized data consisted of time-courses with magnitude spectra identical to those of the data from a living rat, but randomized phase spectra. The following procedure was applied to individual time-courses from the living rat in order to randomize the phases:

1. The discrete Fourier transformation G was obtained for a given time-course g, where G and g have the same length.

2. A random time-course h was generated using MATLAB with its length equal to the original time-course, and its discrete Fourier transform H was obtained.

3. The Fourier transformation W of the phase-randomized time-course w was obtained using the following expression:

$$W(u) = |G(u)|.e^{i\phi(u)} , \qquad \text{where} \quad \phi(u) = \arctan\left(\frac{imag(H(u))}{real(H(u))}\right)$$

4. The phase randomized time-course w was obtained by taking the inverse Fourier transformation of W.

$$w = F^{-1}[W]$$

Results

In all rats, forepaw stimulation resulted in activation in the contralateral SI. The slice showing maximum activation was used as a reference for slice placement for the resting state studies. Figure 10a shows five frames of a typical template obtained with the ROI comprising the whole brain from one of the rat datasets. A window length of 9 s was used for the rat datasets unless otherwise noted, which is nearly twice the propagation time (4.7 s – defined as the time required for the high intensity signal to travel from SII to primary motor cortex) for the waves reported in Chapter 2 and (Majeed, Magnuson et al. 2009), in order to include the negative part of the cycle. Propagation of high intensity from lateral to medial areas is observed in the slices containing sensorimotor cortex (two most anterior slices), confirming the result reported
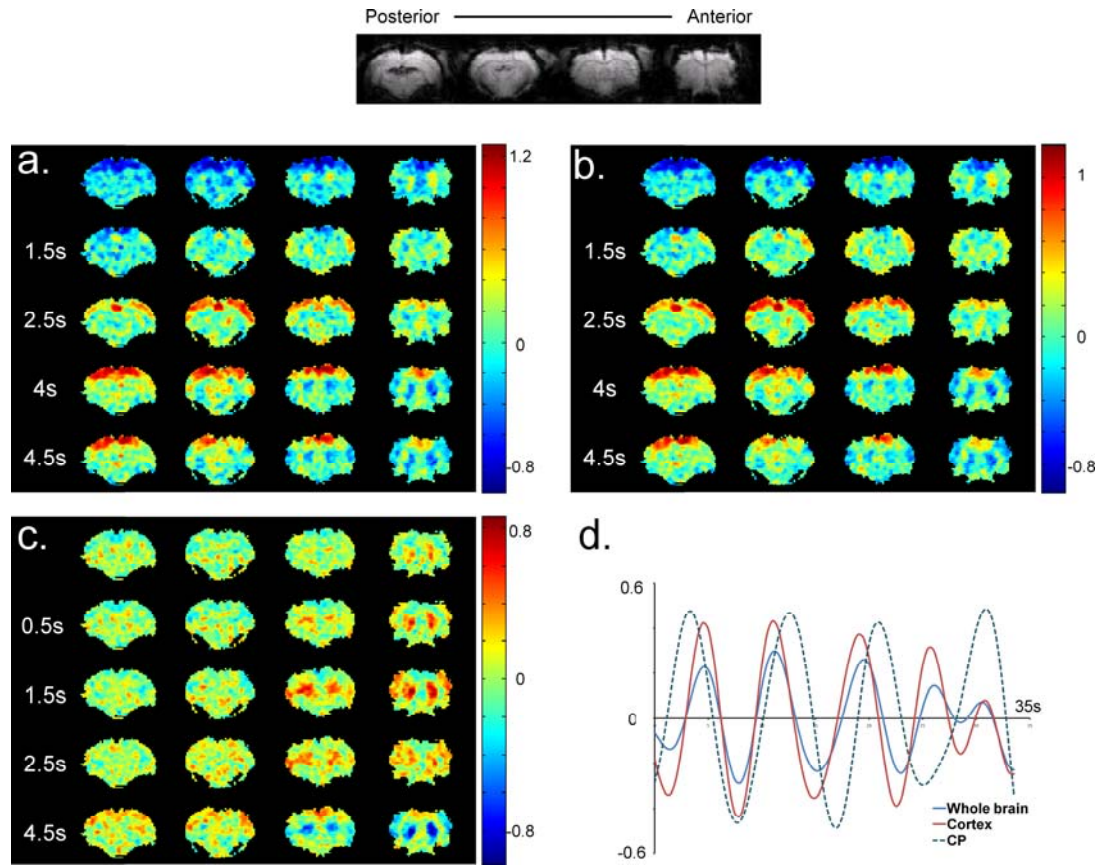
Figure 10: Templates and sliding correlation time-courses for one rat. a) Five frames from a template obtained with an ROI covering the whole brain are shown. A propagating wave of high intensity can be observed in all the slices, followed by a propagating wave of low intensity in the same direction. The second frame (1.5 s) shows the onset of the waves, marked by increased intensity in the lateral cortical areas. The later frames show the propagation of the high intensity towards the medial areas, followed by a wave of low intensity in the same direction. b) The propagation pattern with an ROI covering just the cortex is almost identical to that obtained with the ROI covering the whole brain. The templates obtained with either ROI are highly correlated (cc = 0.87±0.11, averaged over all the rats). c) The spatiotemporal pattern obtained with CP-based ROI shows alternation of positive and negative signal intensities in CP. The increase in BOLD signal is focal in the beginning (0 s) and expands to fill the entire CP. d) Sliding correlation with respective templates for 3 different ROIs. Peaks in the sliding correlation time-course occur at nearly identical time-points for the ROIs covering whole brain and cortex. The correlation time-courses for CP and the other ROIs are sometimes well-aligned, while at other times they are out of phase.

in Chapter 2 and (Majeed, Magnuson et al. 2009) with a different type of anesthesia and lower field strength. In addition, similar waves with similar durations are observed in more posterior slices containing parietal association area and visual cortex. The waves can be observed for 7 of 8 rats (Movie 6). Visual inspection of the templates was used to determine whether the pattern was present.. The only rat dataset not showing this pattern (Rat 5) shows a pattern caused by an imaging artifact (Movie 6). Time-courses from the template were obtained from manually drawn ROIs in the most lateral and most medial areas in the second most frontal slice, which contains sensorimotor regions. The time gap between the transition from negative to positive signal in the most lateral area and transition from positive to negative in the most medial area was defined as the propagation time of the wave. This time averaged 4.8±0.92 s, which is in agreement with the results reported in Chapter 2 and (Majeed, Magnuson et al. 2009). An almost identical pattern (average optimal cc between the templates with either ROI = 0.87±0.11) is detected when an ROI comprising the cortex rather than the whole brain is used for the analysis (Figure 10b, Movie 7). The pattern (defined as visually observable propagation of intensity from the lateral to medial direction in the final template) can be reproducibly observed for all the rats (Movie 7). Half cycle durations (the time between successive positive and negative peaks in the time-course from template for a given region) were recorded to be 3.8±0.42 s and 3.44±0.42 s for ROIs drawn in left and right SI respectively. The speed of propagation of the peak intensity was also measured in the sensorimotor cortex (second most frontal slice). A piecewise linear curve was manually drawn through the middle of the cortex, and the length of the curve was divided by the time-interval between peak intensities in voxels corresponding to the ends of the curve.

The average speed of propagation of the intensity peak was measured to be 4.0±1.34 mm/s. High variability in the calculated speed can be attributed to long sampling time (which reduces temporal precision) as well as inaccuracies in the distance computation due to finite voxel size, distortion and manual delineation of the path of travel.

Figure 10c shows the template obtained from a ROI placed in left and right CP. The main feature of this pattern is an alternation between high and low intensities in bilateral CP. The durations of the half cycle in left and right CP (time between consecutive positive and negative peaks averaged over all the rats for manually defined ROIs in CP) were 3.31±0.26 s and 3.38±0.23 s respectively, similar to the length of the half cycle in SI. Notably, high signal intensity is observed for some cortical areas even though the intensities from the cortex were not used for determining the segments of images that were averaged. In some other cases, the cortex shows low intensity in the averaged template (Movie 8). The pattern was observed in all 8 datasets, based upon visual inspection of the templates (Movie 8).

The sliding correlation time-course shows multiple peaks crossing the threshold (0.2) for all the ROIs, which suggests that the spatiotemporal patterns corresponding to their respective template are repeated several times during the length of the scan (Figure 10d). Average peak-to-peak interval values for the ROIs comprising the whole brain, cortex and CP are 10.22±1.45 s, 8.61±1.15 s and 8.02±0.47 s respectively (sub-threshold peaks were not included). As shown in Figure 10d, the correlation patterns for the whole brain and cortical ROI are almost identical, as expected from the similarity between the corresponding templates. However, the timing of occurrence of the peaks is different for the templates with ROIs placed in cortex and CP as shown in Figure 10d. Consequently,

the templates obtained with CP-based ROIs show lower optimal correlation with the templates based on the other ROIs (whole brain vs. CP: 0.57±0.14, CP vs. cortex: 0.56±0.13), compared with the correlation between the whole brain and cortex-based templates (0.87±0.11). As can be seen in Figure 10d, the sliding correlation time-courses for cortical ROIs and CP ROIs are sometimes well-aligned, while at other times they are out of phase. Our preliminary findings suggest that the low frequency spectrum of the signal from CP is shifted towards higher frequency, compared with the cortex (unpublished findings). Therefore, it is not surprising to observe inconsistent synchrony between the dynamic patterns obtained from these areas. The inconsistent synchrony may account for the inclusion of some cortical areas in the CP templates, depending on which part of the cortical cycle is most commonly aligned with the CP cycle over the duration of the scan.

Although it was not possible to register all the brains due to differences in slice geometry, three datasets with the most similar orientations were registered together using AFNI (Cox 1996), and their templates were aligned in time and displayed as a movie (Movie 9). The visual comparison between the three templates demonstrates consistency of the results across the rats.

In order to assess the reproducibility of the method, the results obtained with different window lengths and seed time-points were compared. Dependence upon seed time-point would suggest either sparseness of the patterns in time, or dominance of different patterns at different times. Dependence on window length might suggest presence of multiple patterns with different durations in the data. Alternatively, the method might be sensitive to the accuracy of the initial guess about the duration of the
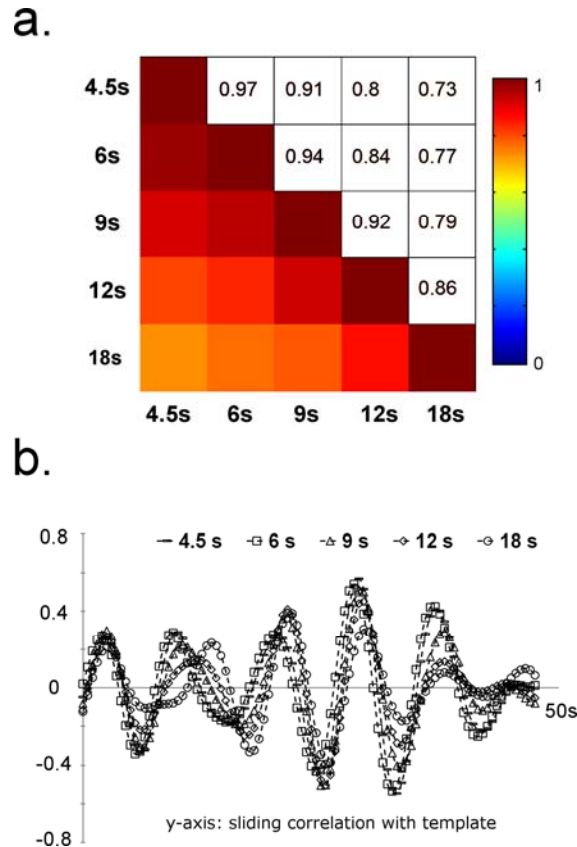
Figure 11: Sensitivity to the initial parameters for rat data. a) Pairwise optimal correlation between the sliding correlation time-courses with different window lengths (averaged over 8 rats). The time-courses are very similar for a wide range of window lengths as indicated by high correlation values between the templates with different window lengths, suggesting that it is not necessary to have accurate a priori knowledge of the temporal extent of the patterns to be detected. b) Sliding correlation time-courses with different window lengths for one rat. Consistent with figure 3a, the time-courses are very similar for a wide range of window lengths.

pattern to be detected, thus making the results dependent upon the window length. Figure 11a shows the pair-wise optimum correlation between the sliding correlation time-courses obtained with different window lengths, averaged over all the datasets (ROI comprising the cortex). The correlation time-courses were used for comparison instead of the templates due to unequal lengths of the templates. The time-courses are very similar

for a wide range of WL (cc > 0.7 for the window lengths ranging from 9 to 36 TRs),

implying that the method is relatively insensitive to the variation in WL. Figure 11b

shows sliding correlation time-courses for 5 different window lengths for one of the rats.

The time-courses are very similar for all 5 window lengths. Pairwise correlation values

(between the templates obtained using an ROI covering the whole brain) at optimum

delay were obtained for 10 different randomly selected seed time-points for all datasets.

The average optimal correlation value of 0.86±0.1 (averaged over all the rats and 40

pairwise comparisons per rat) was obtained, demonstrating the insensitivity of the method

to the seed time-point for the pattern obtained with an ROI placed in the rat cortex.

Figure 12shows a template and plot of sliding correlation for phase-randomized

data with the ROI covering the whole brain. No organized patterns can be seen in the

template (Figure 12a). The sliding correlation function shows some high peaks in vicinity

of the seed time-point (Figure 12b). The amplitude of the peaks rapidly decays to values

close to zero (< 0.1), which suggests that no repeated dynamic patterns are present in the

phase-randomized data.

Summary and Discussion

The propagating waves that we detected in rats are are visually similar to those

identified previously through visual observation, as described in Chapter 2, suggesting

that the waves can be detected reproducibly for different field strengths, TRs and at least

two different anesthesias. Additionally, multislice acquisition used in this study made it

possible to detect any anterior-posterior component of the wave propagation. Our results

suggest that the wave propagation takes place primarily in the lateral to medial direction.

Also, the spatiotemporal pattern involves simultaneous propagation in multiple slices
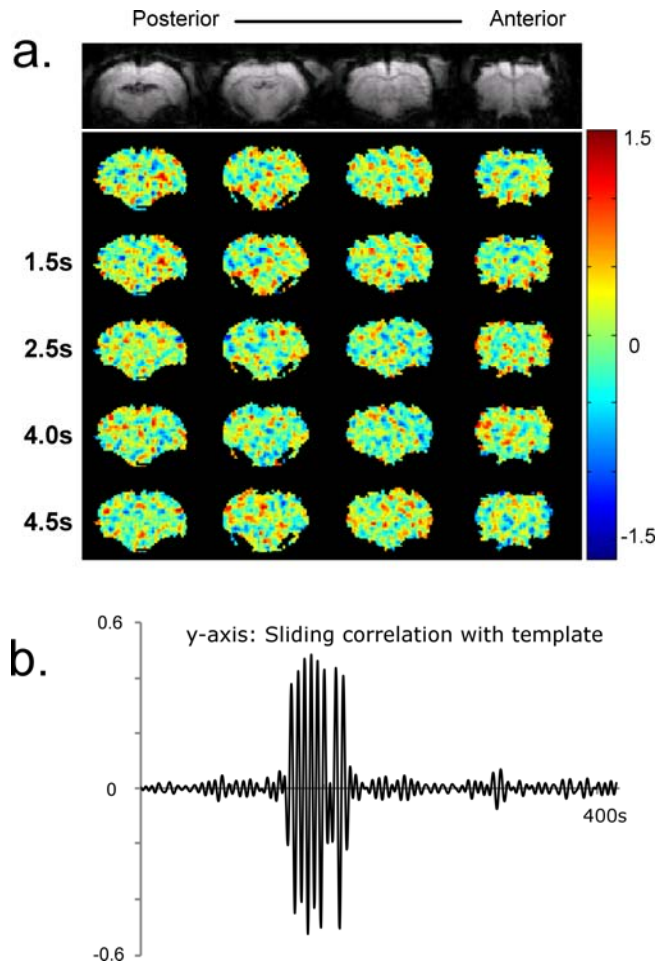
Figure 12: Template and sliding correlation obtained from a phase randomized dataset (dataset with same magnitude spectrum as that of a real dataset, but randomized phases): a) Five frames from the template. No specific patterns can be observed. b) Sliding correlation time-course for the phase-randomized data. The time-course shows high peaks at the time-points only in the vicinity of the seed time-point. Peaks near the seed time-point are expected because the data is temporally smoothed due to filtering. These results suggest that the patterns shown in previous figures are not likely to occur by chance.

ranging from SI to visual cortex. This observation suggests that the underlying

neurovascular event for this pattern either involves long range interaction between the

functional modalities, or is caused by a common source of input or generator (e.g.

47

thalamus). Further experimentation with disruption of activity in the candidates for the possible driver will be needed to make any conclusions in this regard.

The work on rats presented in Chapter 2 utilized a 100 ms TR which guaranteed separation of respiratory and cardiac noise in frequency domain (Majeed, Magnuson et al. 2009). A longer TR (500 ms) was used in this study in order to obtain multislice datasets. Therefore, the first harmonics of respiratory and cardiac noise are aliased into 0-1 Hz range. The typical respiration rate for this study was ~70-80 cycles/minute. However, even frequencies as high as 100 cycles/minute are aliased no lower than 0.33 Hz in the sampled signal, suggesting that respiratory noise is mostly removed by the low-pass filter. Cardiac noise has a much higher frequency and may be aliased into 0-0.2 Hz range. Since the propagation patterns observed in this study are identical to those observed in (Majeed, Magnuson et al. 2009), cardiac noise does not seem to limit the detection of this particular pattern in the data. This is supported by the fact that the cardiac noise is mainly localized to the surface of brains near the draining veins, or base of the brain (Majeed, Magnuson et al. 2009; Williams, Magnuson et al. in press).

The results showed little dependence on initial parameters. Lack of dependence on seed time-point may be attributed to frequent occurrences of the patterns. It may also be attributed to the presence of only one dominant pattern (with higher SNR or greater spatial coverage) in the ROI, which may obscure the less dominant patterns. Independence on window length suggests that it is no essential to have accurate a priori knowledge about the actual length of the patterns.

CHAPTER 5

AUTOMATIC DETECTION OF SPATIOTEMPORAL PATTERNS

IN HUMAN DATA

In this chapter, detection of multiple spatiotemporal patterns in human data is described. Two patterns with different durations are detected and are likely to correspond to two different frequency contributions to LFFs. The dependence of the results on initial parameters is also explored. Our results indicate that the patterns of propagating intensity are not limited to anesthetized rats, and can be seen in humans without the use of anesthesia.

Methods

Imaging

Two groups of human subjects were scanned for this study. The data from the first group was acquired with a short TR (300 ms) to minimize the effects of aliasing of physiological noise and achieve better temporal resolution, while the data from the second group was acquired with long TR (1.5 s) to allow whole brain coverage and inter-subject registration. Imaging was performed on a 3T Siemens scanner using a birdcage head coil. Experiments were conducted according to the Georgia Institute of Technology/Emory University Institutional Review Board (IRB) guidelines approval. The subjects were asked to lie quietly in the scanner with their eyes closed. Anatomical scout scans were acquired in the three orthogonal planes and were used for placement of the slices for the functional scans.

Two runs of EPI image series were acquired from six healthy volunteers (19-22 year old; 3 male, 3 female) with the following parameters: 300 ms TR, 30 ms TE, 3.44 mm × 3.44 mm in-plane resolution, 1600 repetitions, four 5 mm thick horizontal slices (parallel to the line joining anterior and posterior commissures).

Group 2

A single run of EPI image series per subject was acquired with whole brain coverage from 14 healthy volunteers (32-66 year old, 3 male, 11 female), using the following parameters: 1500 ms TR, 30 ms TE, 3 mm × 3 mm in-plane resolution, 276 repetitions, 28 horizontal slices with 4 mm thickness.

Processing

All analyses were performed using Matlab (MathWorks, Natick, MA) unless otherwise noted. The processing steps described below were performed on all the datasets unless specified otherwise. Slice-timing correction and motion correction were performed on all the datasets using AFNI (Cox 1996). Gray matter, white matter and cerebrospinal fluid (CSF) masks were obtained for the human data using Statistical Parametric Mapping (SPM8) software (Wellcome Department of Cognitive Neurology, London, UK). Group 2 human datasets (TR = 1.5 s, whole-brain coverage) were spatially normalized to match the MNI template and resampled to the final voxel size of $3 \times 3 \times 3$ mm^3 using SPM8. A 3D Gaussian kernel (FWHM = 6 mm) was utilized to smooth the Group 2 human data using SPM8. In-plane blurring was performed for the rest of the datasets with a 3×3 Gaussian kernel with $\sigma = 2$ pixels. The time-course from each voxel

was band-pass filtered using FIR filters (0.01-0.08 Hz. Transient time-points were discarded before and after filtering in order to discard transient effects of data acquisition and filtering respectively. Resultant time-courses were mean subtracted, quadratically detrended and normalized to unit variance. Signals from whole brain, CSF and white matter, as well as motion parameters (translation and rotation in 3 dimensions) were regressed out for human data in order to minimize effects of motion, physiological noise and scanner noise.

Group 1 human datasets were analyzed separately for each subject. Human data were analyzed using the algorithm for detection of spatiotemporal patterns (described in Chapter 3) with an ROI comprising the gray matter mask obtained using SPM8. Group analysis was not performed for Group 1. Therefore, qualitative comparison was used for assessing reproducibility across the subjects. Also, some timing parameters of the patterns (discussed later) were compared.

Whole-brain coverage allowed for group analysis for the Group 2 human data. In order to perform group analysis, the preprocessed image series for all the subjects were concatenated together. The template was obtained using the concatenated data (with ROI covering the entire cortex), while ignoring the peaks in the correlation time-course that may have been influenced by the junction between any two datasets. The resultant template was resampled ($2 \times 2 \times 2$ mm^3). Statistical significance of the template in space and time was computed as follows: Intensity values for each spatial location and time were obtained from the image segments averaged to give the final template. Two-tailed t-test was used in order to identify the voxels with intensity values significantly different from zero at a given time (p < 0.001). Isolated voxels in the significance map were

removed by performing erosion followed by dilation ($3 \times 3 \times 3$ kernel consisting of ones).

In order to test sensitivity of the algorithm on the pre-defined parameters, the algorithm was repeated with 1) different values of WL and 2) different values of seed-time point q on the Group 1 human data. The results with different initial parameters were compared. In order to compare the templates, sliding correlation was obtained between the templates (WL' = 3WL, maximum lag = WL) and the maximum value of the sliding correlation was used as the similarity measure between the templates (termed as optimal correlation). Sliding correlation time-courses were compared using the same approach.

Additionally, different frequency sub-bands of the LFFs (0.01-0.04 Hz and 0.04-0.08 Hz) were analyzed separately to detect any spatiotemporal patterns in the respective sub-bands. Details of this analysis are described in the results section.

Results

Group 1

Figure 13a shows five frames for the template obtained for a human dataset (TR = 300 ms, WL = 67 TRs, or ~20 s). Visual inspection of the template reveals switching between the two groups of areas: 1) areas comprising default mode network, and 2) including sensory and motor areas that have been referred to as the dorsal attention network, or task-positive network. These networks have been reported as consistently being anti-correlated in human resting state data (Fox, Snyder et al. 2005; Fransson 2006; Buckner, Andrews-Hanna et al. 2008).
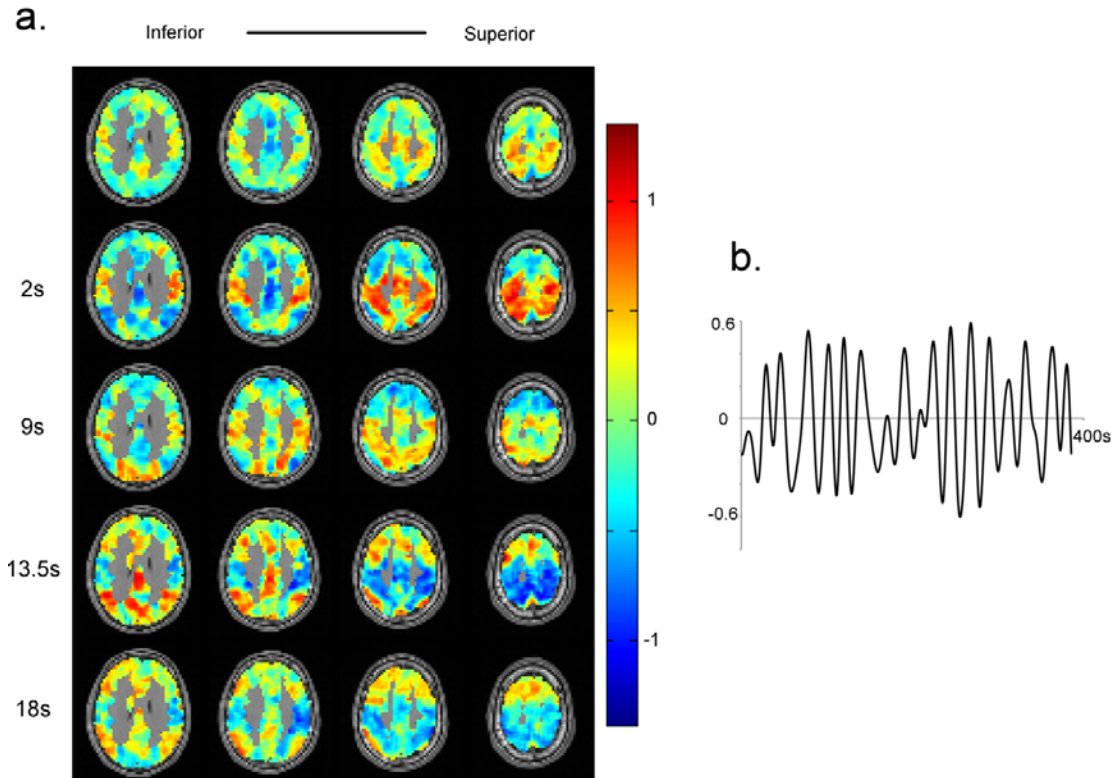
Figure 13: Spatiotemporal patterns and sliding correlation time-courses obtained from a human dataset. a) The pattern shows alteration between the default mode and task-positive/attention networks. At t = 2 s, the attention network shows high signal and the signal from default mode network is reduced. 3rd frame (9 s) shows an intermediate stage between positive and negative signal intensitiy in the attention network marked by reduced signal intensity in the attention network. At t = 13.5 s, positive intensity in the default mode network and negative intensity in the attention network are observed. The signal intensity returns to baseline after some time, as seen in the last frame (18 s). b) The sliding correlation time-course shows multiple peaks which are distributed in time, indicating that the pattern occurs repeatedly during the course of scanning

The pattern occurs several times during the course of the scan, as apparent from the peaks in the sliding correlation function (Figure 13b). However the peak to peak interval (26.41±4.35 s, averaged over all the subjects and sessions) is relatively longer compared with the patterns observed in rats.

The robustness of the method against initial parameters was tested using the approach used for rats. Correlation time-courses show very little variability for a wide range of window lengths (Figure 14a), although relatively low correlation is observed
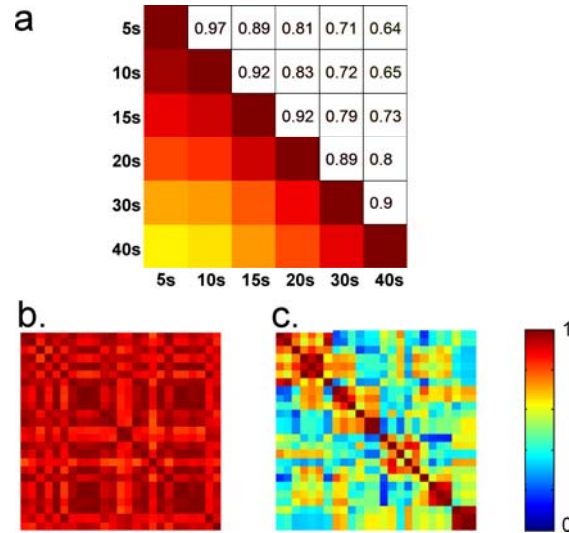
Figure 14: Sensitivity to the initial parameter for human data. a) Pairwise optimal correlation between the sliding correlation time-courses with different window lengths (averaged over 12 sessions). Correlation time-course for 20 s window length is very similar to those obtained from window lengths ranging from 5 s to 40 s (cc > 0.8). Therefore it is not necessary to have exact knowledge about length of the pattern to be detected. However, relatively low correlation is observed between longest and shortest window lengths. b) Correlation matrix representing pairwise optimal correlation between the templates obtained using 25 random starting points for a human dataset. The templates obtained with different seed time-points are highly correlated for this dataset. c) Correlation matrix obtained from another human dataset (the data points were re-ordered in order to emphasize the clusters of similar templates). For this particular dataset, not all the templates with random seed-points show high correlation. b and c suggest that depending upon the data set, the seed time-point may or may not have an impact on the results.

between the correlation-time-courses obtained using extreme values of window length (5s and 40s). However, in contrast with the results obtained for rats, the templates do not always show high correlation for different seed time-points with a fixed window length (Figure 14b and c). Therefore the template obtained from a given dataset with a fixed window length is not unique, which complicates the comparison of the patterns within and between the subjects. In order to resolve this issue, templates were obtained from 25 different seed time-points for each dataset (window length = 67 TRs or ~20 s). The

54

templates were clustered based upon the pairwise optimal correlation values using hierarchical clustering. The seed time-point corresponding to the "most central" template belonging to the biggest cluster was chosen for within and between subject comparison, where the "most central" template is defined as the one with the maximum average correlation with rest of the templates belonging to the biggest cluster. The seed time-point selected using this method resulted in the templates containing the pattern described above. The seed-time point for the template displayed in Figure 13 was chosen using the same approach. Qualitative comparison suggests that the pattern shown in Figure 13 (consisting of switching between default mode and task-positive networks) was obtained for 11 out of 12 sessions (Movie 10). Session 1 for subject 6 is the only session for which this pattern was not observed (Movie 10). Based upon qualitative comparison, the results are reproducible within the subject for 5 out of 6 subjects (subjects 1-5). The average optimal correlation between the templates obtained from the two sessions was 0.3 ± 0.12. Half cycle times for average signals from ROIs drawn in task-positive and default mode were 9.6 ± 1.12 s and 9.95 ± 1.0 s respectively (averaged over the 11 sessions with consistent spatiotemporal pattern). Speed of propagation was not calculated for humans because the propagation path is not clearly defined due to the convoluted cortex. The average switching time (defined as the time between positive peak intensities in the default mode and task-positive networks) was 10.5 ± 1.45 s (calculated using manually drawn ROIs, 11 sessions exhibiting consistent pattern used).

Group 2

In order to perform group analysis, the preprocessed image series for all the subjects were concatenated together. Clustering of templates with random seed-points

was used to select the seed, as described above. The templates for 50 random seed time-points were obtained (WL = 13 TRs or ~20 s). The templates thus obtained were clustered as described above and the most central seed time-point in the biggest cluster was used for rest of the analysis. The statistical significance of the template in space and time was computed using a t-test in order to identify voxels that showed statistically significant positive / negative intensity at a given time, as described in the methods section (p < 0.001). Since the data was acquired with whole brain coverage, it was possible to visualize the dynamic pattern for other orientations (Figure 15, Movie 11). Visual inspection of the template shows alteration between the default mode and anti-correlated task-positive networks. Close examination, however, reveals propagation of intensity from some focal points, especially in the sagittal plane (indicated on Figure 15a using white arrows) over several seconds. The first propagation starts with appearance of high intensity in parieto-occipital sulcus and fusiform gyrus (Figure 15a, 0s, columns 5 and 4 from the left). The high intensity propagates to other areas including precuneus, cuneus, and visual cortex. The second propagation starts after the first pattern and is marked by propagation of negative signal intensity within the prefrontal cortex towards more frontal areas (column 5, 3 s). Propagation of negative intensity from the posterior cingulate cortex (PCC) to the adjacent areas is also observed (column 7, 3 s). Additionally, propagation of high intensity from premotor cortex to more anterior parts of the frontal cortex, and probably posterior cingulate cortex (column 7, 6 s) is observed. This template is shown with more time-points and slices in Movie 11. ROIs were drawn in the default mode network and task-positive network and the switching time (time between maximum signal intensities in default mode network and task-positive network)
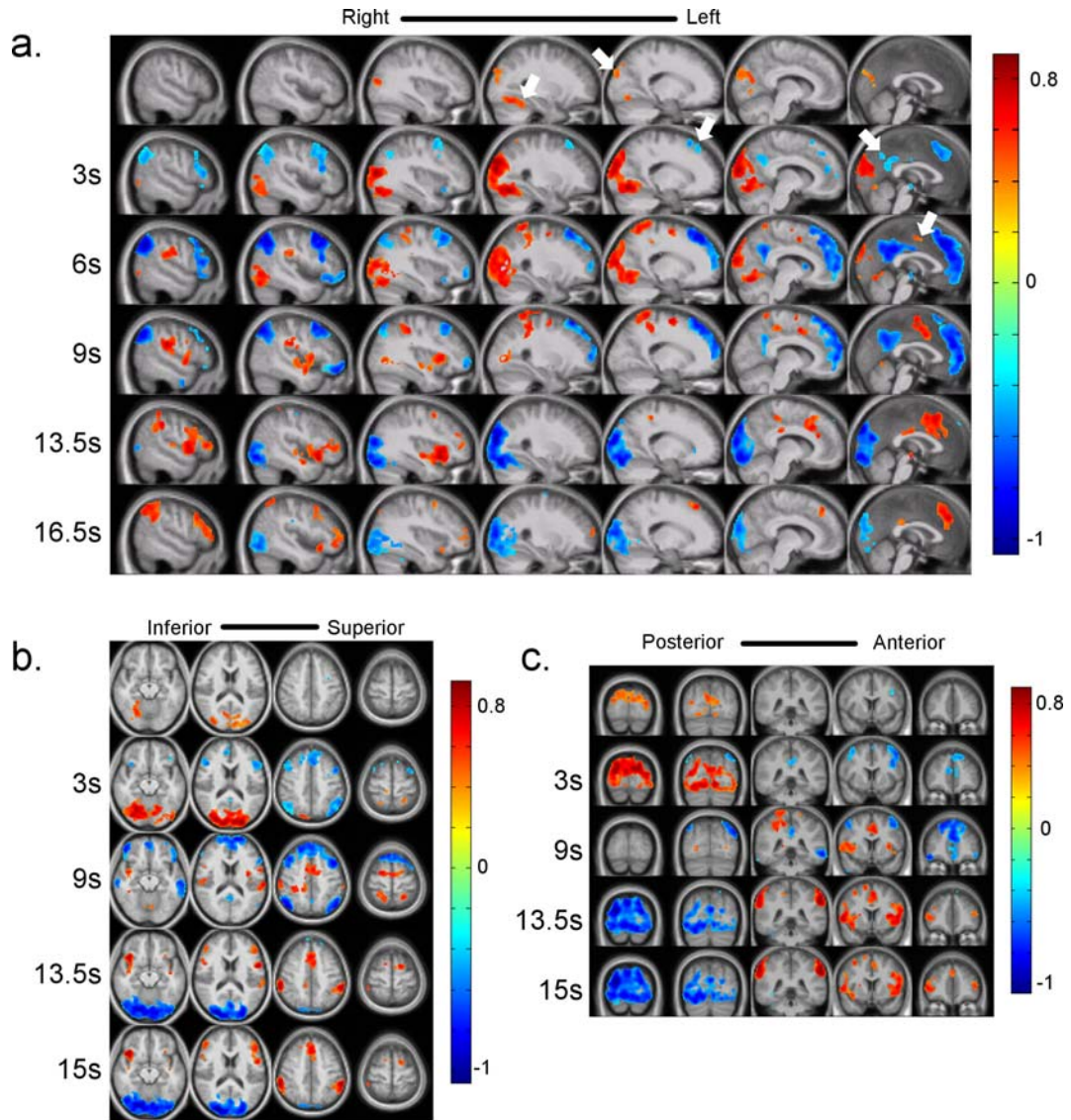
Figure 15: Frames from the template obtained using group analysis in three different planes. The color bars represent average z-scores for a given voxel at a given time in the template. Switching between the task-positive and default mode networks can be observed in all three orientations (a, b, c). Closer inspection reveals propagation of signal from focal points to the other brain areas (especially in the sagittal plane). The "sources" of the signal propagation are indicated by white arrows on figure 7a. Propagation of positive signal change can be seen starting from fusiform gyrus and parieto-occipital sulcus (0 s, columns 4 and 5) as well as medial premotor cortex (6 s, column 7). The propagation of negative signal change can be seen from the areas including medial prefrontal cortex (column 5, 3 s), posterior cingulate cortex (column 7, 3 s). The propagation can continue for more than 10 s (e.g. the propagation of positive signal change from premotor cortex). A clearer visualization of these propagation patterns can be seen in Movie 6. More investigation into finding the significance of such "sources" can provide us a new insight into the origin of the low frequency fluctuation.

was calculated. The switching time obtained for the template for group data was 10.5 s.

Half cycle times for default and task-positive networks had the same value of 10.5 s

(measured using the approach described earlier). All these measurements are within one

standard deviation from those obtained from Group 1 data.

It was impractical to assess inter-subject reproducibility for Group 2 data because
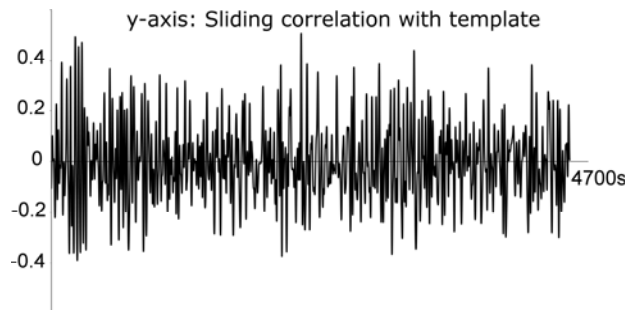
Figure 16: Sliding correlation time-course for the template obtained from the concatenated data (14 subjects). The occurrence of high peaks is not restricted to a small window in time, suggesting that the template obtained from the concatenated data represents a pattern that occurs reproducibly across the subjects.

high SNR templates could not be obtained for individual datasets due to limited number

of repetitions per dataset. Instead, reproducibility of the detected pattern was assessed for

smaller subgroups. The templates were obtained for the following subgroups: subjects 1-

5; subjects 6-10; subjects 10-15; subjects 1, 3, 5, 7, 9; subjects 2, 4, 6, 8, 10; and subjects

6, 8, 10, 12, 14. Thirty random seed time-points were used for each subgroup and the

most central template from the biggest cluster was selected for each subgroup for

comparison with the template obtained using all 14 subjects. The templates obtained for

the subgroups showed high optimal correlation (0.64±0.13) with the template obtained

from all 14 subjects, suggesting that the pattern detected using group analysis is not dependent upon the specific set of subjects selected for the analysis.

This particular pattern detected for 0.01-0.08 Hz component is referred to as pattern 1 later in the text.
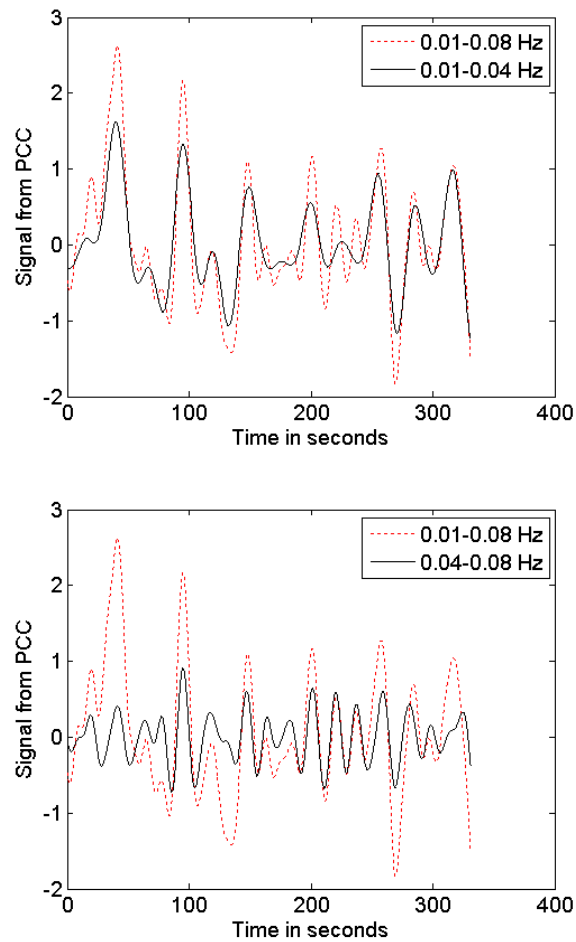
Figure 17: Signals obtained using different filters for 300ms TR human data. 0.04-0.08 Hz shows the faster fluctuations (2nd row) which are overwhelmed by the 0.01-0.01 Hz contribution (1st row)
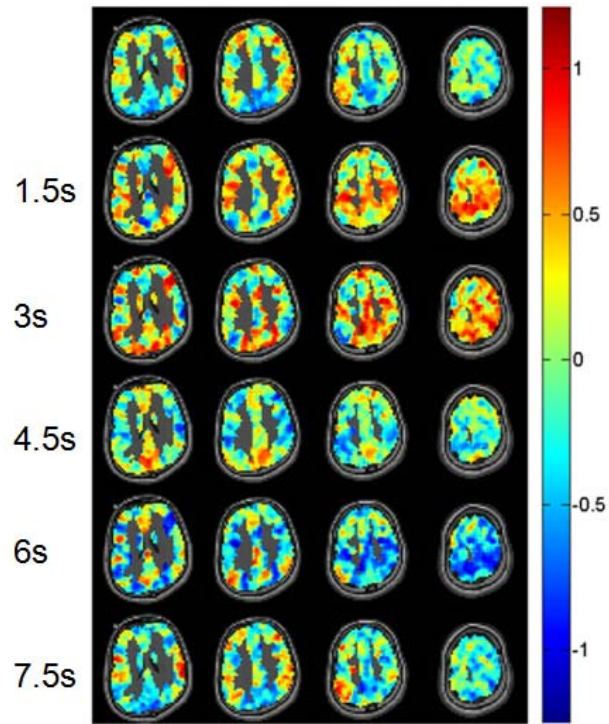
Figure 18: Template obtained for 0.04-0.08 Hz component of LFFs for a Group1 human subject. The pattern consists of switching between default and task-positive networks, similar to the pattern obtained for 0.01-0.08 Hz component. High intensity in task-positive network is seen between 1.5 and 3 seconds, whereas high intensity in the default mode network is seen between 6 and 7.5 seconds from the first frame. However, these changes occur at a much smaller time-scale compared with the pattern with 20s window length (0.01-0.08 Hz filter).

Spatiotemporal Patterns for Sub-bands in LFFs

Virtually all functional connectivity studies performed on humans utilize a frequency range between 0 and 0.1Hz. However, it is possible that there might be different contributions in the LFFs which might be separated in frequency domain, as suggested by presence of two low frequency peaks with different characteristics in rat data. Figure 17 suggests that this point of view may be valid. The plots show signal from

PCC after application of different filters. 0.01-0.04 Hz component of the signal (Figure 17, top) provides a good approximation of the slow variations in the LFFs (0.01-0.08 Hz) in PCC. However, there are faster oscillations that are not captured by 0.01-0.04 Hz signal (e.g. Figure 17, top, ~175s). 0.05-0.08 Hz component of the signal captures those faster oscillations, emphasizing the low amplitude details that are otherwise overwhelmed by the 0.01-0.04 Hz component. These results suggest that the patterns detected for 0.01-0.08 Hz might be caused by 0.01-0.05 Hz component of the signal due to its high relative amplitude, and it might be interesting to analyze the two sub-bands separately. Figure 18 shows the pattern observed in 0.04-0.08 Hz component of the signal (~10s window length) for Group 1 human data (300 ms TR). This pattern corresponds to the most central template belonging to the biggest cluster obtained after clustering the templates with 25 different random seed time-points (as described before). Therefore, it corresponds to the most robustly detectable pattern in the 0.04-0.08 Hz component of the fluctuations. The pattern shows switching between default mode and task-positive networks, consistent with that observed in 0.01-0.08 Hz component of the signal. However, the time required for switching between the task positive and default mode networks (~6s) is much shorter in comparison.

Group analysis was applied to the whole-brain data using the 0.04-0.08 Hz filter and ~10s window length. Preprocessed image series for all the subjects were concatenated. Templates obtained using 50 random seed time-points were clustered. Figure 19 shows the pattern corresponding most central template for the biggest cluster. Consistent with the pattern obtained from 300ms TR data, switching between default and attention mode is observed, with a switching time of 6 seconds (the switching time was

computed as described in the previous section). In addition shorter switching time, the time required for signal to propagate between the brain areas is much shorter, as compared with the pattern obtained for 0.01-0.08 Hz component (based upon visual assessment). Interestingly, this pattern shows negligible involvement of the visual cortex, as opposed to Pattern 1 (0.01-0.08 Hz, ~20s window length), which shows much greater involvement of the visual cortex. 0.01-0.05 Hz component of the signal was analyzed in similar way with ~20 s window length. The resultant pattern showed high similarity with that obtained using 0.01-0.08 Hz component of the signal (cc = 0.75).

The pattern detected for 0.01-0.04 Hz component is referred to as pattern 2 later in the text.
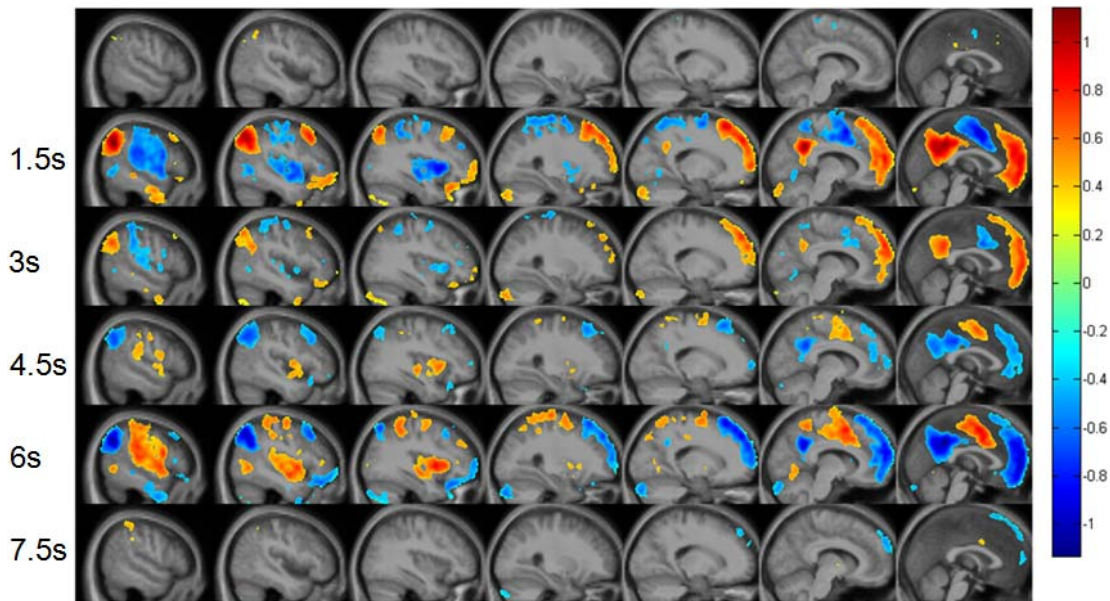

Figure 19: Pattern obtained with 10s window length and 0.04-0.08 Hz component for Group 2 data. Propagation of intensity is not as clearly observable as for the pattern with 20s window length (0.01-0.08 Hz range) due to much faster switching (switching time of 6s vs 10.5s for the previous pattern).

Summary and Discussion

The work presented in this chapter demonstrates that multiple spatiotemporal patterns can be detected in the LFFs in human fMRI data. The patterns are consistent within and between the subjects based upon visual assessment and consistency of the timing parameters (half-cycle time and switching time) and can be reliably detected using single-subject analysis as well as group analysis. The patterns obtained using short (300ms) as well as long (1.5s) show switching between the default and task-positive network with similar half-cycle and switching times, suggesting that the patterns are not likely to be caused by aliasing of physiological noise.

The primary pattern obtained using conventional frequency range (0.01-0.08 Hz) shows switching between default and attention networks. The group analysis reveals propagation of signal intensities from focal starting points. Analysis using multiple frequency bands suggested presence of two sub-bands in the signal. The sub-bands were analyzed separately, which resulted in detection of a faster propagation pattern. These results suggest that multiple spatiotemporal patterns may be present in the overlapping brain regions. Future multimodality research as well as behavioral experiment will help in establishing the neural and behavioral significance of the patterns.

Our results are in agreement with the anti-correlation observed between default and task-positive networks, e.g. (Fox, Snyder et al. 2005). Therefore, anti-correlated changes in the intensity of these networks can be inferred from traditional functional connectivity analysis. However, the propagation of the signal, as reported in this chapter, may not be detected using traditional analysis. Also, Group analysis suggests that the

observed patterns have a finite duration, before or after which no significant BOLD

activity is observed. Traditional methods cannot reveal such details.

CHAPTER 6

CONTRIBUTION OF THE PATTERNS TO LFFS

As noted in the previous chapters, multiple spatiotemporal patterns can be detected in rat and human data. This raises the question of whether contributions of different patterns to LFFs can be estimated. Estimation of these contributions can be important for several reasons. First, it is possible that different patterns might correspond to different processes/neural rhythms and estimation of their contribution to LFFs might provide us with a better understanding of brain function in different conditions. Secondly, some patterns might be obscured by stronger patterns, and removal of contribution due to the stronger patterns may help us detect the weaker pattern.

Methods for Estimating Contribution of the Patterns to LFFs

Two approaches to estimate the contribution of a spatiotemporal pattern are described in this section. The spatiotemporal pattern is described by the sliding correlation $r_0(n)$ and the final template $T_0(x, y, z, n)$. Expanded window length WL_0 is used to obtain $T_0(x, y, z, n)$. $I(x, y, z, n)$ represents the preprocessed image series.

Method 1

An intuitive way to obtain the contribution of a specific spatiotemporal pattern to LFFs would be to identify the peaks in $r_0(n)$ and to "place" the pattern at the peak locations. Mathematically, this operation can be described as convolution, and computed as following:

$$\bar{I}_{approx}(x, y, z, n) = \sum_{m} u_0(m).T_0(x, y, z, n - m)$$

where

$$u_0(n) = \begin{cases} r_0(n), & r_0(n) > r_0(n \pm 1) \\ 0, & otherwise \end{cases}$$
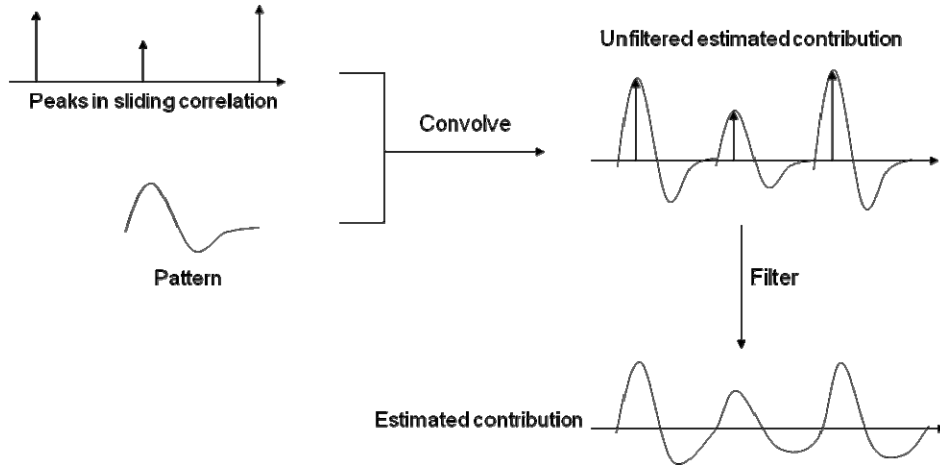
Figure 20: Method 1 for estimating the contribution of the patterns to LFFs. The method is explained for a pattern consisting of a single time-course for simplicity. x-axis represents time in all the plots. First, the pattern is convolved with a single consisting of impulses at the peak locations in the sliding correlation. The height of the impulses is the same as height of the impulses The result of convolution (labeled as unfiltered estimated contribution). A low pass filtered is applied to the unfiltered estimated contribution to obtain the estimated contribution.

$\bar{I}_{approx}(x, y, z, n)$ represents an approximation of the component of the original time-series that can be explained by a particular pattern. However, it is likely to have temporal discontinuities, which should not be present in otherwise low frequency fluctuations. Therefore, $\bar{I}_{approx}(x, y, z, n)$ is temporally filtered with a low-pass filter with impulse response $h(n)$ to smooth the time-courses and remove any discontinuities/high frequency component, followed by detrending:

66

$$\hat{I}_{approx}(x, y, z, n) = \sum_m \bar{I}_{approx}(x, y, z, m).h(n - m)$$

$\hat{I}_{approx}(x, y, z, n)$, when appropriately scaled, can be used as the approximation of

contribution of the pattern to the image series:

$$I_{approx} = \hat{I}_{approx} \cdot \left(\frac{1}{K_2} \sum_{(x,y,z) \in S} \sum_n I(x, y, z, n).\hat{I}_{approx}(x, y, z, n) \right)$$

$$\text{Where} \quad K_2 = \frac{1}{\sqrt{\left(\sum_{(x,y,z) \in S} \sum_n \hat{I}_{approx}(x, y, z, n)^2 \right)}}$$

Method 2

As mentioned before, the Method 1, when used without smoothing the result of

convolution contains discontinuities. Although filtering can be used to eliminate the

discontinuities, the specifications of the filter might affect the results. Also, a priori

knowledge about the corresponding pattern (such as average distance between the peaks,

estimated frequency range) is needed to design the filter. Approach 1 can be extended

such that the template is "placed" at every time point after being weighted by the sliding

correlation value at a given time point. Mathematically, this represents convolution

between the sliding time-course $r_0(n)$ with the template $T(x, y, z, n)$:

$$\hat{I}_{approx}(x, y, z, n) = \sum_m r_0(m).T_0(x, y, z, n - m)$$

This approach is similar to that used when reconstructing the signal from wavelet

coefficients using inverse wavelet transform. The resultant image series does not have

discontinuities, therefore no temporal smoothing is required.

$$I_{approx} = \hat{I}_{approx} \cdot \left(\frac{1}{K_2} \sum_{(x,y,z) \in S} \sum_n I(x,y,z,n) . \hat{I}_{approx}(x,y,z,n) \right)$$

Where $\quad K_2 = \dfrac{1}{\sqrt{\left(\displaystyle\sum_{(x,y,z) \in S} \sum_n \hat{I}_{approx}(x,y,z,n)^2 \right)}}$
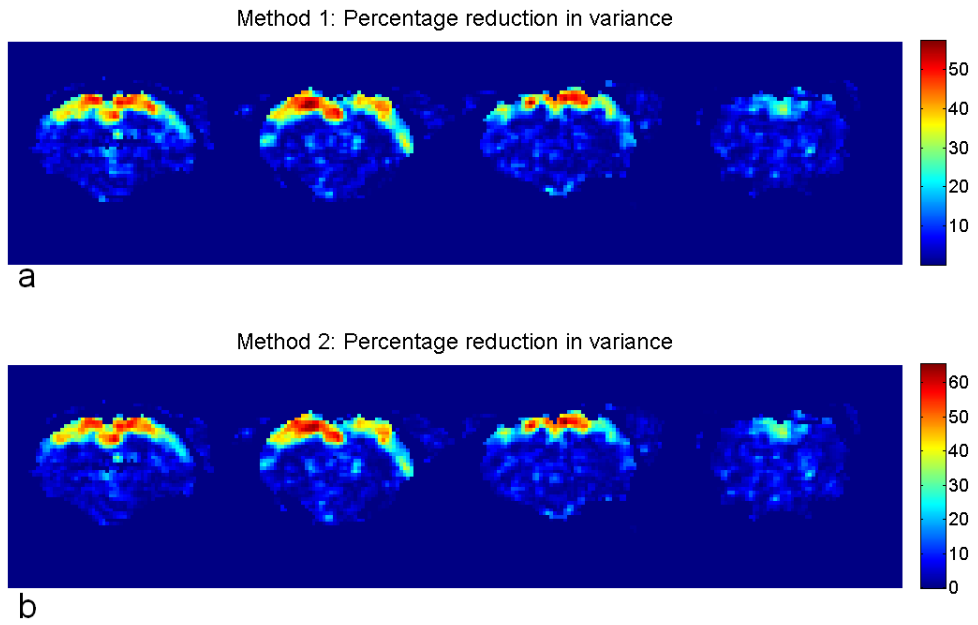
Figure 21: Percentage reduction in variance of LFFs after removing the contribution of the spatiotemporal pattern using two different methods. The spatial pattern of reduction of the variance after subtracting the estimated contribution is very similar for both methods. However, more variance is reduced when the estimated contribution obtained using method 2 is subtracted from the preprocessed image series.

Comparison between the Methods

Figure 21 shows percentage reduction in the variance of the LFFs after subtracting the approximated contribution of the pattern with whole brain ROI (I_{approx})

from the original preprocessed image series, *I*. As apparent from the figure, the pattern of

reduction of variance is almost identical for relatively more intuitive Method 1, and more

complicated method 2. Method 1 results in smaller reduction in the variance of the LLFs,

though. This difference might be caused by relative inaccuracy of the Method 1 due to

filtering used for removing the discontinuities. Method 2 is used for obtaining the results

described later because it results in smooth approximation of the image series without

requiring filtering with manually selected parameters.

Contribution of the Patterns to the LFFs

Multislice Rat Data

Figure 22 shows reduction in variance of the time-courses in the image series

caused by subtraction of the contribution of the templates obtained for different ROIs. As

seen in the first two rows of the figure, the patterns obtained with cortical and whole-

brain ROI contribute towards the variance of LFFs with identical magnitude. However,

the pattern obtained with an ROI placed is CP primarily contributes towards the

fluctuations in CP itself. Average percentage reduction in cortex was observed to be

25.67±5.88% and 5.6±2.04% after regressing out the contribution of templates with ROIs

placed in cortex and CP respectively. The corresponding values for CP were 7.51±4.36

and 34.51±13.93 respectively.
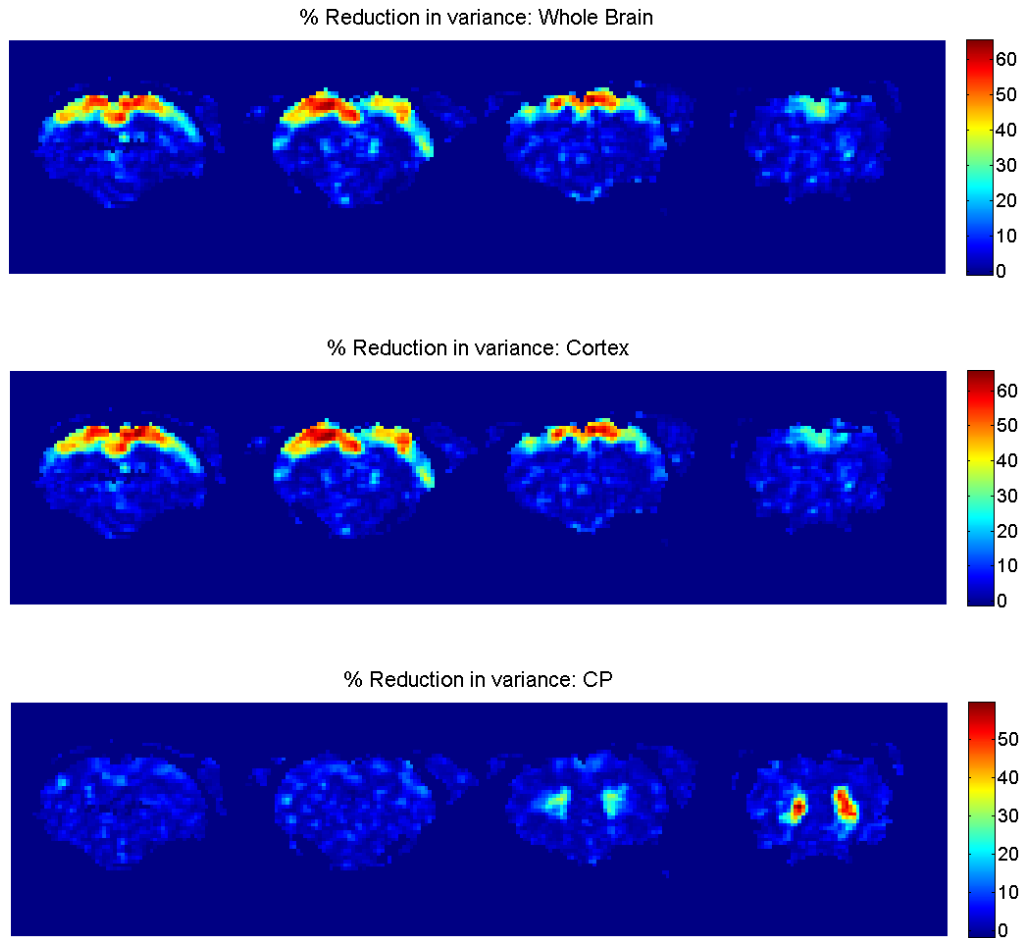
Figure 22: Percentage reduction in variance after regressing out the contribution of the patterns obtained with ROIs placed in the whole brain, cortex and CP. Regression of the patterns obtained with cortical and whole brain ROIs results in reduction in the variance of fluctuations in the cortex, consistent (rows 1 and 2). Only CP shows strong reduction in the magnitude of LFFs when the pattern obtained with CP-based ROI is regressed out (row 3).

Human Data

As described in Chapter 5, two spatiotemporal patterns (referred to as Pattern 1 and Pattern 2 henceforth) with different time-scales can be detected in single slice as well as multislice data. Pattern 1 is the most robustly detectable pattern obtained from the data filtered with 0.01-0.08 Hz range using 20 seconds long window length, whereas Pattern 2

is detected after limiting frequency contributions to 0.04-0.08 Hz and using 10 seconds window length.
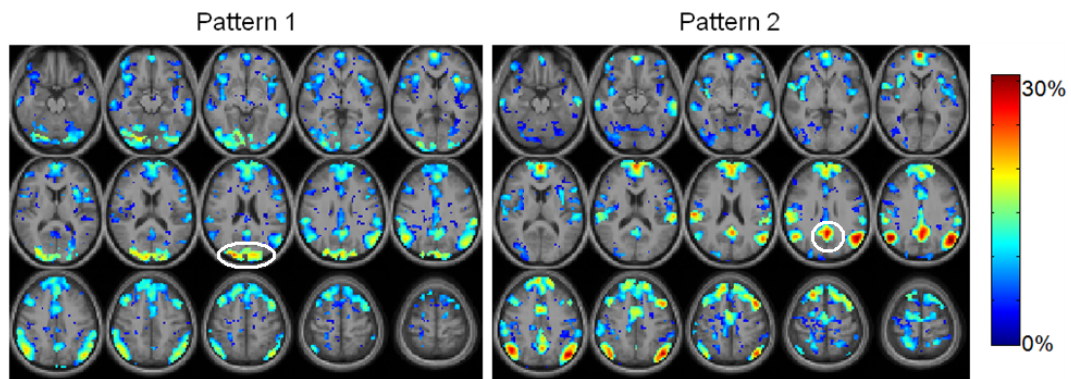
Figure 23: Reduction in variance after removing the contribution due to different patterns in human data. The spatial distribution of reduction in the variance is pattern dependent. For example, significant reduction in the variance of LFFs is observed in the visual cortex (encircled on the left figure) when pattern 1 is regressed out, but not pattern 2. Removal of contribution due to pattern 2 results in greater reduction in the variance of fluctuations in the areas comprising default mode network e.g. PCC (encircled on the right figure)

Figure 23 shows percentage reduction in variance after removing the contribution due to the patterns ($p < 0.01$). Visually detectable differences in the spatial distribution of variance due either pattern are observed. For example, Pattern 2 has greater contributions towards the fluctuations in areas including sensorimotor cortex, inferior part of parietal cortex and PCC. Pattern 1 shows much greater contributions towards the fluctuations in the visual cortex compared with Pattern 2.
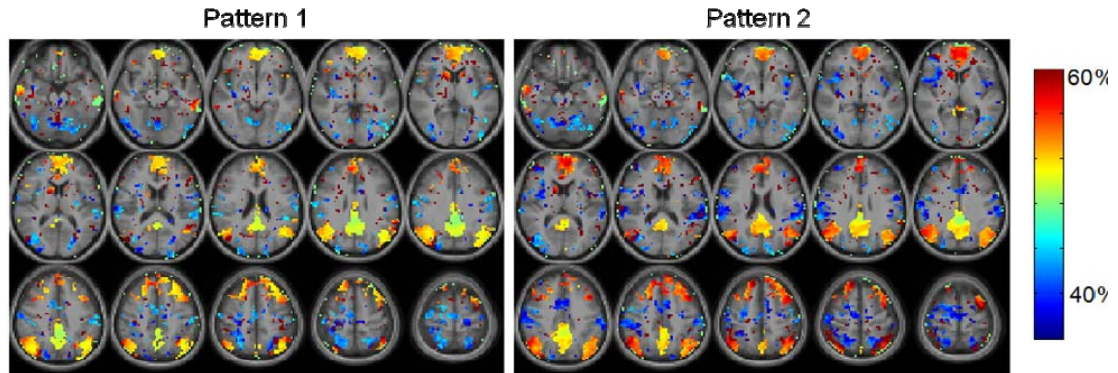
Figure 24: Reduction in cross correlation with PCC after regressing out the contribution due to different pattern. Greater reduction in correlation coefficient is observed when the contribution of pattern 2 is removed.

Figure 24 shows percentage reduction in absolute value of correlation coefficient after removing contribution due to each pattern. The maps show less difference in the spatial distribution of reduction in correlation coefficient. However, overall greater reduction in correlation coefficient is seen after removal of the contribution of Pattern 2.

Application: Iterative Approach for detecting New Patterns

Estimation and removal of the spatiotemporal patterns can be used as part of an iterative approach for detecting other patterns. This approach can be especially helpful in order to detect multiple patterns in the data that might otherwise not be detectable due to sub-optimal ROI selection as well as relative dominance of a pattern over the others. It is not always possible to know the spatial extent of the patterns to be detected. Therefore it is not always possible to select the optimal ROI for pattern detection. Selection of an ROI that comprises area containing multiple patterns can result in detection of only the most dominant pattern. For example, only cortical propagation pattern is observed for multislice rat data when whole brain is used as an ROI (Figure 10a). However, after

analyzing CP separately, a spatiotemporal pattern specific to CP can be observed (Figure 10c). This suggests that the cortical pattern is probably the most dominant pattern, and therefore may have a much stronger influence on the peaks in sliding correlation, thus obscuring the other patterns. One solution to this problem is to remove the contribution of already detected patterns and to detect the patterns in the residual data. This process can be repeated iteratively in order to detect the patterns that might otherwise not be detected.
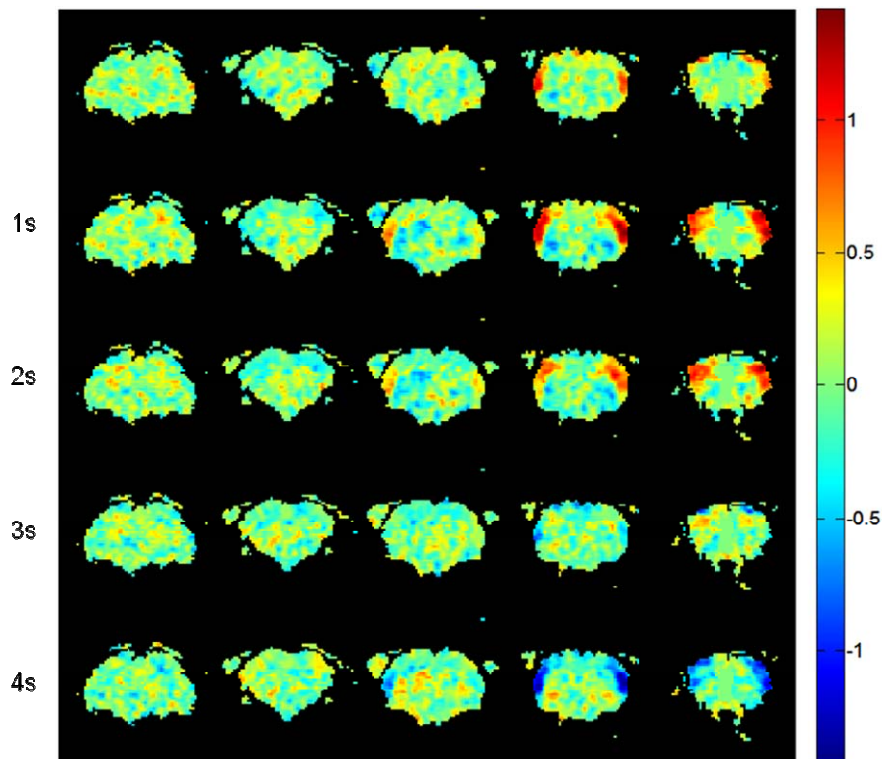
Figure 25: Five frames from Secondary spatiotemporal pattern in the rat cortex. This was obtained after regressing out the contribution of the previous pattern obtained with cortical ROI from the data. The pattern shows changes in intensity in SII and anterior somatosensory areas. No propagation occurs in the other cortical areas.

This approach was applied to the multislice rat data to detect a new pattern in the rat cortex. The contribution of the propagating pattern corresponding to the cortex (Figure 10b) was removed from the image data and the pattern finding algorithm was applied to the residual data using multiple seed time-points. The resultant templates were clustered. Figure 25 shows the pattern corresponding to the biggest cluster in the residual data. Interestingly, the new pattern is different from the previously detected pattern with cortical and whole brain ROIs. This pattern is restricted to more anterior somatosensory areas as well as SII, and does not show any involvement of parietal or visual cortices. This result demonstrates the utility of the iterative approach described above for detection new patterns.

Summary and Discussion

An approach for estimating the contribution due to the spatiotemporal patterns is described in this Chapter. The approach is used to estimate the contribution of the spatiotemporal patterns detected in rats and humans (as described in Chapters 4 and 5). For rat data, the estimated contribution due to the spatiotemporal patterns detected for cortex and CP-based ROIs were specific to the respective ROIs. Whole brain human data (Group 2) were analyzed in the same fashion and the results demonstrate different spatial specificity of the contribution due to the two patterns with different time scales.

Our results indicate that removal of already detected pattern may make it easier to detect the otherwise undetected patterns. This approach can be very important for developing an exploratory approach for detecting the spatiotemporal patterns without accurate prior information about the spatial territories of the individual patterns.

DISCUSSION

The research presented in this thesis demonstrates the presence of repetitive spatiotemporal patterns of BOLD fluctuations and presents an approach to detect these patterns automatically. The timing of occurrence of the patterns can also be extracted, thus preserving spatial as well as temporal information in the data. The patterns were first detected in high temporal resolution rat data (100ms). To better characterize the dynamics of the BOLD signal, we developed a novel approach to detect repeated spatiotemporal patterns in the fMRI data. The method has been tested for robustness to changes in initial parameters, and can be applied to multislice human and rat data to detect the patterns that are reproducible within and between subjects. The results indicate presence of multiple spatiotemporal patterns in the rat and human data at different TR, field strengths and anesthetic agents, and suggest the possibility of presence of multiple contributions in the LFFs. These contributions might have different neural/non neural origins and further research is needed to establish their basis. The presence of multiple contributions to the LFFs highlights the importance of analyzing different frequency sub-bands in the LFFs separately.

Algorithm for Spatiotemporal Pattern Detection

Ideally, a functional imaging modality should be able to provide information about both spatial and temporal aspects of brain activity. In other words, it should be able to provide information about brain function with high spatial and temporal resolution. Compared with other functional modalities, fMRI provides excellent spatial and moderate temporal resolution. However, the amount of information that can be obtained

from fMRI data is limited by several factors, SNR being one of them. In order to

overcome this limitation, averaging over time is a method used extensively in fMRI

studies exploring the response to a task or stimulus. This allows us to identify the areas

that, on average, show an increase or decrease in activation under the time-window

representing the stimulus or task. Although this averaging does not preserve trial-to-trial

variability or ongoing changes in brain activity that might be unrelated to the task, it

allows us to effectively increase the SNR, and provides some spatial and temporal

information at the cost of details which are averaged out. This approach relies on

manipulation of brain activity at known times. (i.e.: blocks or events). Improvement of

SNR by averaging for functional connectivity data, on the other hand, is non-trivial of the

fact that the brain activity is not controlled by any external stimuli. As a result,

conventional functional connectivity analysis techniques rely on detecting a relationship

between signals from brain regions over the entire length of acquisition. This approach

identifies brain areas that show correlated BOLD fluctuations across the session, but

compromises precise temporal information. The algorithm developed for the detection of

spatiotemporal patterns demonstrates that averaging is possible for functional

connectivity data because the data consists of the repetitive spatiotemporal blocks. We

can then study when these blocks occur in time, thereby preserving the temporal

information.

Although the detected patterns are in agreement with the previous functional

connectivity studies, additional information (e.g. propagation of BOLD signal, duration

of the individual patterns) can be obtained using our method.

The algorithm developed for detection of spatiotemporal patterns relies on the assumption that the patterns occur several times during the course of data acquisition. Another assumption is that a chunk of consecutive images starting at a random time captures whole or part of a spatiotemporal pattern of interest with fairly high probability. Therefore, this approach for detecting spatiotemporal patterns has certain limitations. First, it can only be used for reproducible patterns, as sufficient averaging may not be achieved for isolated events. However, the validity of isolated events, even if detected, would remain questionable due to SNR limitations. Second, the method uses a pre-specified window length and starting point. Although the examples shown in the later sections suggest that the results are not influenced by window length over a wide range of values, it is conceivable that some patterns might have significantly different duration compared with the window length used, and thus may not be detected. In addition, the seed time-point used for the process might influence the final template obtained by the method. These problems can be alleviated by using this method as an exploratory approach. Templates can be obtained for a wide range of window lengths and seed time-points. For a given seed time-point, the templates can be clustered into the groups representing spatiotemporal patterns with different durations. For a given window length, the clusters would represent spatiotemporal patterns with almost the same duration that occur at different times.

The examples presented in this thesis demonstrate different ways in which this algorithm can be used as an exploratory method. As described above, one approach is to cluster the results obtained with multiple seed time-points and window lengths. Another approach would be to utilize different ROIs for analysis. The ROIs can be based upon

anatomical sub-divisions in the brain as well as functional networks. The patterns

obtained for rat data are extracted using this approach. As presented in Chapter 5,

removal of the contribution of previously detected patterns can reveal new patterns. This

approach may be helpful in exploring the patterns without perfect knowledge of the

patterns to be detected. It can also be useful to detect the patterns that might share the

same anatomical territories, but may have different relative dominance. Finally, as

reported in Chapter 4, analysis of different sub-bands can be used in order to explore the

spatiotemporal patterns in the brain.

Rat Data

α-chloralose Anesthesia

The implications of the research performed on α-chloralose anesthetized rats

(Chapter 2) are two-fold: 1) It identifies visually detectable spatiotemporal patterns in the

resting state BOLD data that are not revealed by the conventional analysis 2) It

demonstrates the presence of multiple peaks in the low frequency band, showing different

spatiotemporal characteristics and functional connectivity. Minimal preprocessing steps

(temporal filtering, spatial blurring and normalization) are performed prior to the visual

inspection. Therefore the propagation pattern is not likely to be an artifact introduced by

the preprocessing.

Low frequency fluctuations in neural activity, cerebral blood flow, and blood

oxygenation levels have been observed in both humans and animals (Golanov,

Yamamoto et al. 1994; Obrig, Neufang et al. 2000; Leopold, Murayama et al. 2003).

However, the links between these phenomena have barely been explored and the inter-

relations may be complex, particularly in anesthetized animals. In addition to changes in

78

blood oxygenation level and cerebral blood volume, the signal intensity of the EPI images acquired in this study is also highly sensitive to changes in cerebral blood flow, due to the short repetition time. It is possible to envision, then, a situation in which signal fluctuations in one frequency range (e.g., LF1) reflect widely coherent oscillations in blood flow (possibly due to vasomotion) while signal fluctuations in another range (LF2) reflect changes in the oxygenation level of blood, possibly linked with neural activity, that are more localized to highly connected cortical areas. This hypothesis is purely speculative because the relationship between neural activity and cerebral blood flow is highly dependent upon anesthesia, and no studies measuring electrical activity and blood flow have been performed in the α-chloralose anesthetized rat to our knowledge. Multimodality studies are needed to test the hypothesis.

 If the peaks can be attributed to different aspects of the brain's function, it may be that the relative magnitude of the two peaks is highly sensitive to the level of anesthesia, accounting for the variability seen in this study. Previous work has shown that functional activation increases with time after anesthesia is changed from halothane to α-chloralose, and therefore the extent to which halothane washes out prior to imaging might be a factor that determines the relative contribution of LF1 and LF2 (Austin, Blamire et al. 2005). Experimentation with controlled variation in anesthesia depth and time after initial dose of the anesthetic agent can be used to investigate this issue.

 Propagation patterns for LF1 seem unlikely to reflect coordinated neural activity between areas of the brain because of the lack of functional specificity. The primary propagation pattern for LF1 moves inward from the surface of the brain, and high signal appears across the entire cortex at once. Simultaneous fMRI-electrophysiology studies

with multiple electrodes over the surface of brain will be needed in order to investigate this hypothesis.

The propagation patterns for LF2 are potentially more interesting. SI, SII and MI are all strongly connected anatomically, and the bilateral onset of the waves is suggestive of coordinated activity. Previous studies have reported fluctuations in cerebral blood flow at approximately 0.1 Hz, attributed to vasomotion (Golanov, Yamamoto et al. 1994). The waves of cerebral blood flow occurred simultaneously in both hemispheres, and were relatively high in amplitude (~20% (Golanov, Yamamoto et al. 1994)). Low frequency oscillations in neural activity have also been observed (Leopold, Murayama et al. 2003) and the close coupling of cerebral blood flow and increases in neural activity during stimulation suggests that they are related. Thus, the propagating waves observed in this study may reflect the spatiotemporal dynamics of low frequency oscillations in neural activity, although multimodality experimentation is required to prove this point of view. This idea is supported by recent work from Shmuel and Leopold (Shmuel and Leopold 2008), which showed that the BOLD signal from the visual cortex in monkeys was correlated with band limited power of gamma band using simultaneously recorded fMRI and electrophysiological signal. The correlation was strongest at a lag of approximately 6 s, and the pattern of correlation propagated away from the electrode with a time scale of seconds. While the animal preparation used in these studies was very different, the similarities between the propagation of correlated BOLD responses and the spontaneous waves observed here are striking.

Other possible explanations for the waves observed here are less convincing. The presence of propagating waves raises the spectre of spreading depression, i.e. spreading

depolarization across the cortex (Leao 1944). However, the waves observed in this study occur at a much shorter time scale in comparison, and all animals were physiologically stable.

Our findings suggest that the two low frequency peaks contain different information and may have different physiological origins. Both connectivity maps and propagation patterns are dependent upon the frequency range chosen for analysis. These results motivate in-depth investigation of frequency-band selection for functional connectivity studies. In an interesting parallel to these results, Obrig et al. reported the presence of two low frequency peaks (~0.04 Hz and ~0.1 Hz) in blood oxygenation level measurements made using near infrared spectroscopy in human subjects (Obrig, Neufang et al. 2000), suggesting that the phenomenon described in this manuscript may not be limited to anesthetized rodents.

The observed spatiotemporal patterns are also not likely to be due to the aliased components of the physiological contributions. First, the high sampling rate resulted in alias-free sampling of the primary components of both cardiac and respiratory rhythms. Secondly, the power maps for these peaks do not overlap completely with the low frequency peaks of interest. Although there is some overlap between the power maps of low frequency signals and respiratory contribution, those maps do not look identical and there are cortical areas where low frequency peaks can be seen in absence of any significant physiological peaks. Neither can these patterns be attributed to scanner noise, because they were not observed in the data obtained from the dead rat. Also, it is unlikely that the scanner noise should be restricted to the cortical region only.

It is interesting to note that physiological noise does not appear to have a major impact on functional connectivity studies in rats. The connectivity maps with a seed placed in were qualitatively similar to those obtained by other groups using longer repetition times (Lu, Zuo et al. 2007; Pawela, Biswal et al. 2008; Zhao, Zhao et al. 2008). However, localized contributions from respiratory and cardiac noise were observed in our data and may be a confounding factor in functional connectivity studies of other brain regions, particularly those near large vessels or the ventricles.

This study utilizes single slice data because the short TR did not allow the acquisition of more images. Consequently, our data cannot reveal the full spatiotemporal propagation of the traveling waves. The primary direction of travel of the LF2 waves may not be SII to MI, as it appears in this study, because single slice data can capture only a projection of the wave motion. Further work on medetomidine anesthetized rats (Chapter 3) addresses this issue by using a longer TR (500ms) and acquiring more slices, and indicates that the primary direction of the propagation is indeed lateral to medial.

The presence of the propagating waves has implications in regard to interpretation of functional connectivity maps. Although functional connectivity between SI and SII is reduced due to time lag (manifested as propagation of intensity from SII to SI), the propagation of the signal from SI to SII (and MI) suggests some kind of communication or "functional connection". Observation of such events in the resting state BOLD data is expected to have a significant impact on how we interpret functional connectivity.

The detection of propagating waves of MRI signal fluctuations that may reflect slow changes in electrical activity naturally leads to speculation about whether other dynamic neural events can be detected with MRI. While the task-related BOLD response

has been shown to reflect changes in neural activity, particularly in local field potentials, previous attempts to link functional connectivity measurements with electrophysiology have proven hard to interpret. Even recent work in animals has pointed to potentially different sources for BOLD signal correlation. Lu et al presented indirect evidence linking LFFs with delta band power in somatosensory cortex of anesthetized rodents, while Shmuel and Leopold recently showed that the MRI signal reflected changes in the gamma band power of local field potentials using implanted electrodes in the visual cortex of anesthetized monkeys (Shmuel and Leopold 2008). Studies have also been performed in human subjects in order to investigate neural correlate for LFFs and functional connectivity. Goldman et al reported negative correlation between BOLD and alpha band power in multiple cortical regions of awake humans using simultaneous acquisition of EEG and fMRI (Goldman, Stern et al. 2002). Another simultaneous EEG-fMRI study by Mantini et al (Mantini, Perrucci et al. 2007) suggests that multiple frequency bands are related to the LFFs, and that the frequency spectra is different for different functional networks. A recently published human study by He et al utilizes electrocorticography and fMRI in the patients with intractable epilepsy and indirectly suggests that both slow cortical potentials (< 4Hz, overlapping with delta band) and gamma band power are related to LFFs in BOLD in wakefulness and rapid-eye-movement sleep (He, Snyder et al. 2008). Only slow cortical potentials showed a correlation pattern similar to that of LFFs in other states of sleep. In another study, the results varied within scans from the same subjects, suggesting that the relationship between LFFs and the EEG signal may vary depending on the current state of the subject (Gonçalves, de Munck et al. 2006). In general, the area of the brain that is studied, the

83

relative sensitivity of the electrical recording techniques, and the state of the subject (awake, asleep, or anesthetized) might explain some of the differences in the findings. These studies highlight the need for further research addressing the issue of the neural origin of the LFFs. Animal studies may provide the missing link. The ability of MRI to distinguish time-varying features such as periods of elevated cortical bursting will be limited by the temporal resolution of the imaging technique and the vascular response, the relative signal to noise of the signal of interest, the spatial extent of the activity, and the amount of time for which the activity persists.

Medetomidine Anesthesia

The propagating waves that we detected in rats are qualitatively similar to those identified previously through visual observation, as described in Chapter 2 and reported in (Majeed, Magnuson et al. 2009). Additionally, multislice acquisition used in this study made it possible to detect any anterior-posterior component of the wave propagation. The results suggest that the wave propagation takes place primarily in the lateral to medial direction. Also, the spatiotemporal pattern involves simultaneous propagation in multiple slices ranging from SI to visual cortex. This observation suggests that the underlying neurovascular event for this pattern either involves long range interaction between the functional modalities, or is caused by a common source of input or generator.

Although the frequency range of interest for LFF analysis in humans is fairly well established (Biswal, Yetkin et al. 1995; Fox, Snyder et al. 2005; Fox, Corbetta et al. 2006; Vincent, Snyder et al. 2006), different groups have used different frequency ranges for the analysis of rat data (Lu, Zuo et al. 2007; Pawela, Biswal et al. 2008; Zhao, Zhao et al. 2008; Majeed, Magnuson et al. 2009; Williams, Magnuson et al. in press). Several of

these studies have utilized a frequency cutoff of 0.08-0.1 Hz, which matches that used for

human data analysis (Lu, Zuo et al. 2007; Pawela, Biswal et al. 2008; Zhao, Zhao et al.

2008). These studies utilized low sampling rates that do not allow detailed analysis of the

frequency components in the low frequency range. As reported in Chapter 2, short TR

(100ms) data was utilized for alpha-chloralose anesthetized rats to demonstrate the

presence of higher frequencies of interest in 0-0.2 Hz range, also reported in (Majeed,

Magnuson et al. 2009). Two low frequency peaks (LF1: 0.01-0.025 Hz Hz, LF2: 0.12-

0.17 Hz) were detected in the data obtained from α-chloralose anesthetized rats. LF1

(isolated using a low-pass filter with 0.05 Hz cutoff) showed global connectivity patterns,

suggesting that it may not contain useful information about functional networks. LF2,

however, showed specific bilateral connectivity patterns, suggesting that frequency

components with f > 0.08-0.1 Hz may carry information about the functional connectivity

networks in rats. Further work in medetomidine anesthetized rats shows that the higher

frequency fluctuations are not merely a consequence of the α-chloralose anesthesia. First,

the power spectrum analysis suggests that high power can be seen in 0-0.2 Hz range even

without aliasing of primary components of repiratory and cardiac noise (Magnuson,

Majeed et al. 2009; Majeed, Magnuson et al. 2009; Williams, Magnuson et al. in press).

Bilateral reduction in power in 0-0.2 Hz range is observed as a result of continuous

unilateral forepaw stimulation, suggesting functional significance of the fluctuations in 0-

0.2 Hz range (Majeed, Magnuson et al. 2009). In contrast with the two distinct peaks seen

in at least some of the α-chloralose anesthetized rats, a broad low frequency spectrum

was observed for medetomidine anesthetized rats (Magnuson, Majeed et al. 2009;

Majeed, Magnuson et al. 2009; Williams, Magnuson et al. in press). This suggests that

the use of different anesthetic agents might result in variation in the relative contribution of different vascular or neural factors to the LFFs and raises the question of whether the band-pass filtered component in the data obtained from medetomidine anesthetized rats is equivalent to LF2 peak as observed in α-chloralose anesthetized rats (Majeed, Magnuson et al. 2009). We believe that 0.08-0.2 Hz component of LFFs in medetomidine anesthetized rats has a dominant LF2 contribution because spatiotemporal properties of 0.08-0.2 Hz component are same for both types of anesthesia. Additional evidence comes from a study showing a peak at ~0.2 Hz in the cerebral blood volume (CBV)-weighted functional data obtained from medetomidine anesthetized rats (Magnuson, Majeed et al. 2009). That clear peak was not observed for BOLD weighted images obtained from the same rats. The spatiotemporal properties for the CBV-weighted data were in agreement with those reported for α-chloralose anesthetized BOLD data (data not shown). Although lower frequency contributions (LF1) were shown to exhibit global correlation for α-chloralose anesthtiszed rats, it is conceivable that they might contain relevant information about the functional networks for a different anesthesia. This point of view is supported by the specific connectivity patterns reported for medetomidine anesthetized rats obtained with cutoff frequencies of 0.1 Hz or 0.08 Hz (Pawela, Biswal et al. 2008; Zhao, Zhao et al. 2008). We have focused on the analysis of LF2 in this study because it allows direct comparison to our previous study (Majeed, Magnuson et al. 2009) and confirms that similar spatiotemporal dynamics can be observed at a lower field strength and under a different anesthesia. The contribution in the lower frequency range for the medetomidine anesthetized rats will be analyzed separately as part of future work.

Human Data

The research performed on human data suggests the presence of multiple

spatiotemporal patterns in the LFFs. Pattern 1 (Figure 15) was detected using the

conventional frequency range used for functional connectivity analysis for humans (0.01-

0.08 Hz) and ~20 s window length, whereas Pattern 2 (Figure 18) was detected using a

window length of ~10 s after filtering the data with 0.05-0.08 Hz filter. The contributions

of these patterns to the variance in LFFs are differently distributed in space Figure 22.

Recent work (Seeley et al., 2007) suggests the ventral attention network can be

further subdivided into two networks based on intrinsic connectivity: a salience network,

containing dorsal anterior cingulate and frontoinsular cortices, and a right-lateralized

executive network, comprised of lateral prefrontal cortex and lateral parietal cortex. This

subdivision may also be reflected temporally in the Pattern 1, as regions within the

salience network (Figure 15, 9-13.5 s in red) appear to peak in intensity before those in

the executive network (Figure 15, 13.5-16.5 s in red). The temporal relationship between

these putative sub-networks may speak to the internal connectivity and "drivers" within

these systems, and should be investigated further. Examinations such as these further

highlight the utility of approaches that investigate spatiotemporal dynamics of BOLD

fluctuations.

The spatiotemporal patterns detected for the short and long TRs show alteration

between default and task-positive networks. The switching time between default and

attention network obtained using both TRs are in excellent agreement. As removal of

primary components of respiratory and cardiac noise was possible with a TR of 300 ms, it

can be concluded that the pattern is not caused by aliased components of respiratory or

cardiac noise. However, it is possible that physiological noise may alter the spatial spread of the pattern, as suggested by the reduction in spatial extent of correlation caused by regression of respiratory contribution (Birn, Diamond et al. 2006). Simultaneous acquisition of fMRI and physiological signals will be used in future studies in order to study the effect of removal of these cycles on the spatiotemporal pattern.

While other factors, including vasomotion, can contribute towards the BOLD signal in addition to the local hemodynamics associated with the neural activity, there is mounting evidence suggesting neural and behavioral relevance of the LFFs (Goldman, Stern et al. 2002; Gonçalves, de Munck et al. 2006; McNamara, Tegenthoff et al. 2007; Liu, Zhu et al. 2008). Therefore, it is reasonable to hypothesize a neural basis of the patterns presented in this paper. The link between propagation of the BOLD signal and possible propagation of neural activity has yet to be established. The difference in hemodynamic delays between different brain regions can result in the propagation patterns even in the absence of propagating neural activity. A multimodality approach involving fMRI and electroencephalography (EEG) will be needed to establish the neural/non-neural basis of the propagation patterns.

Implications for Functional Connectivity and Neuroimaging Research

This study has several implications for functional connectivity research. The approach developed in this study provides a way to detect the underlying spatiotemporal patterns that give rise to the LFFs. It would be interesting to explore other patterns in the data and find their relative contribution to the LFFs. It has been suggested that LFFs might be caused by a "neuronal driver", sending a common input to "functionally connected" areas (Drew et al., 2008). Although this speculation has yet to be confirmed

experimentally, our technique to study spatiotemporal propagation provides a promising way to identify potential candidates for the driver (or drivers) of LFFs, or the areas receiving direct input from the drivers. For example, lateral to medial propagation of the signal in rodents might suggest that the lateral areas are either the drivers of the LFFs, or they receive the input from the drivers (e.g. thalamus), which further spreads across the cortex. If these areas act as the starting points for a slow modulation of neural activity, the energy demands of adjacent areas would increase as their activity increased, resulting in an increase in BOLD signal that follows the propagation path of the activity. However, as discussed earlier, difference in hemodynamic delays can induce propagating patters in BOLD signal that may not be related with propagating neural activity. Therefore, further investigation with multiple modalities is needed to test this hypothesis.

This novel approach not only identifies the spatiotemporal patterns, but also given information about their occurrence in time. This information can be especially useful for behavioral paradigms. For example, future research can be performed in order to identify correspondence between occurrence of different patterns and performance on a behavioral task. Additionally, correspondence between the relative contribution of different patterns and behavior or disease state can be investigated. An advantage of using the relative contributions instead of other measures, such cross correlation, is that the ratio between the contributions due to different patterns is less likely to be affected by different levels of white noise and may provide a measure which may require little processing for calibration between sessions and subjects. These future applications are purely speculative and further experimentation is required before any strong conclusions can be made in this regard.

Conclusions

This work demonstrates that the spatiotemporal patterns of BOLD fluctuations are a robust phenomenon, occurring in different species (rats and humans) and detectable at a wide range of field strengths and TRs. The presence of multiple spatiotemporal patterns is demonstrated using visual detection and a novel pattern detection method. The patterns detected using the two approaches are in agreement for rats and persist for different anesthetic agents, TRs, contrast mechanisms (CBV and BOLD). The same patterns are observed for TRs short enough for sampling the physiological noise, as well as longer TRs for humans as well as rats, suggesting that the physiological noise is not the source of these patterns. Our analysis suggests the presence of at least two low frequency contributions in rat as well as human data, which has potential implications for the analysis and interpretations of the LFFs. Future work is needed in order to establish neural and behavioral significance of these findings.

In conclusion, the work presented in this thesis has the potential of being an important contribution towards fMRI research. It not only pushes the limits on the information that can be obtained from BOLD fMRI data, but also adds a new dimension to analysis of LFF.

REFERENCES

Austin, V., A. Blamire, et al. (2005). "Confounding effects of anesthesia on functional activation in rodent brain: a study of halothane and a-chloralose anesthesia." Neuroimage **24**(1): 92-100.

Birn, R., J. Diamond, et al. (2006). "Separating respiratory-variation-related fluctuations from neuronal-activity-related fluctuations in fMRI." NeuroImage **31**(4): 1536-1548.

Biswal, B., A. Hudetz, et al. (1997). "Hypercapnia reversibly suppresses low-frequency fluctuations in the human motor cortex during rest using echo-planar MRI." J Cereb Blood Flow & Metab **17**: 301-308.

Biswal, B., F. Yetkin, et al. (1995). "Functional connectivity in the motor cortex of resting human brain using echo-planar MRI." Magn. Reson. Med. **34**: 537-541.

Brinker, G., C. Bock, et al. (1999). "Simultaneous recording of evoked potentials and T*2-weighted MR images during somatosensory stimulation of rat." Magnetic Resonance in Medicine **41**(3): 469-473.

Buckner, R. L., J. R. Andrews-Hanna, et al. (2008). "The brain's default network." Ann. N. Y. Acad. Sci. **1124**: 1-38.

Chang, C. and G. H. Glover (2009). "Time-frequency dynamics of resting-state brain connectivity measured with fMRI." NeuroImage **50**(1): 81-98.

Cohen, J. D., S. D. Forman, et al. (1993). "Activation of the prefrontal cortex in a nonspatial working memory task with functional MRI." Human Brain Mapping **1**(4): 293-304.

Cordes, D., V. Haughton, et al. (2000). "Mapping functionally related regions of brain with functional connectivity MR imaging." AJNR Am. J. Neuroradiol. **21**(9): 1636-1644.

Cordes, D., V. Haughton, et al. (2002). "Hierarchical clustering to measure connectivity in fMRI resting-state data." Magn. Reson. Imaging **20**(4): 305-317.

Cox, R. W. (1996). "AFNI: software for analysis and visualization of functional magnetic resonance neuroimages." Comput. Biomed. Res. **29**(3): 162-173.

de Pasquale, F., S. Della Penna, et al. (2010). "Temporal dynamics of spontaneous MEG activity in brain networks." Proceedings of the National Academy of Sciences **107**(13): 6040.

Drew, P. J., J. H. Duyn, et al. (2008). "Finding coherence in spontaneous oscillations." Nature **11**(9): 991-993.

Fox, M., M. Corbetta, et al. (2006). "Spontaneous neuronal activity distinguishes human dorsal and ventral attention systems." Proc. Natl. Acad. Sci. U.S.A. **103**(26): 10046-10051.

Fox, M., A. Snyder, et al. (2005). "The human brain is intrinsically organized into dynamic, anticorrelated functional networks." Proc. Natl. Acad. Sci. U.S.A. **102**(27): 9673-9678.

Fransson, P. (2006). "How default is the default mode of brain function? Further evidence from intrinsic BOLD signal fluctuations." Neuropsychologia **44**(14): 2836-2845.

Garrity, A., G. Pearlson, et al. (2007). "Aberrant" default mode" functional connectivity in schizophrenia." Am J Psychiatry **164**(3): 450.

Glover, G., T. Li, et al. (2000). "Image-based method for retrospective correction of physiological motion effects in fMRI: RETROICOR." Magnetic Resonance in Medicine **44**(1): 162-167.

Golanov, E., S. Yamamoto, et al. (1994). "Spontaneous waves of cerebral blood flow associated with a pattern of electrocortical activity." Am. J. Physiol. Regul. Integr. Comp. Physiol. **266**(1): 204-214.

Goldman, R., J. Stern, et al. (2002). "Simultaneous EEG and fMRI of the alpha rhythm." Neuroreport **13**(18): 2487-2492.

Gonçalves, S., J. de Munck, et al. (2006). "Correlating the alpha rhythm to BOLD using simultaneous EEG/fMRI: Inter-subject variability." Neuroimage **30**(1): 203-213.

Grady, C., M. Furey, et al. (2001). "Altered brain functional connectivity and impaired short-term memory in Alzheimer's disease." Brain **124**(4): 739.

Greicius, M., B. Flores, et al. (2007). "Resting-state functional connectivity in major depression: Abnormally increased contributions from subgenual cingulate cortex and thalamus." Biol Psychiatry **62**(5): 429-437.

Greicius, M., B. Krasnow, et al. (2003). "Functional connectivity in the resting brain: A network analysis of the default mode hypothesis." PNAS **100**(1): 253-258.

Hampson, M., B. Peterson, et al. (2002). "Detection of functional connectivity using temporal correlations in MR images." Hum Brain Mapp **15**(4): 247-262.

He, B., A. Snyder, et al. (2008). "Electrophysiological correlates of the brain's intrinsic large-scale functional architecture." Proc. Natl. Acad. Sci. U.S.A. **105**(41): 16039.

Hu, X., T. Le, et al. (1995). "Retrospective estimation and correction of physiological fluctuation in functional MRI." Magnetic Resonance in Medicine **34**(2): 201-212.

Johnston, J., S. Vaishnavi, et al. (2008). "Loss of resting interhemispheric functional connectivity after complete section of the corpus callosum." J Neurosci **28**(25): 6453.

Keilholz, S., A. Silva, et al. (2004). "Functional MRI of the rodent somatosensory pathway using multislice echo planar imaging." Magn Reson Med **52**(1): 89-99.

Kim, D. S., T. Q. Duong, et al. (2000). "High-resolution mapping of iso-orientation columns by fMRI." nature neuroscience **3**(2): 164-169.

Leao, A. (1944). "Spreading depression of activity in the cerebral cortex." J Neurophysiol **7**(6): 359-390.

Leopold, D., Y. Murayama, et al. (2003). "Very slow activity fluctuations in monkey visual cortex: Implications for functional brain imaging." Cereb Cortex **13**(4): 422-433.

Li, S., B. Biswal, et al. (2000). "Cocaine administration decreases functional fonnectivity in human primary visual and motor cortex as detected by functional MRI." <u>Magn Reson Med</u> **43**: 45-51.

Liu, X., X.-H. Zhu, et al. (2008). "Tightly coupled spontaneous EEG and CBF signals in the anesthetized rat brain." <u>Proc. Int. Soc. Magn. Reson. Med. Sci. Meet. Exhib.</u> **16**: 755.

Liu, Y., C. Yu, et al. (2007). "Whole brain functional connectivity in the early blind." <u>Brain</u> **130**(8): 2085.

Lowe, M., M. Phillips, et al. (2002). Multiple sclerosis: Low-frequency temporal blood oxygen level-dependent fluctuations indicate reduced functional connectivity-initial results. <u>Radiology</u>, RSNA. **224:** 184-192.

Lu, H., X. Golay, et al. (2003). "Functional magnetic resonance imaging based on changes in vascular space occupancy." <u>Magnetic Resonance in Medicine</u> **50**(2): 263-274.

Lu, H., Y. Zuo, et al. (2007). "Synchronized delta oscillations correlate with the resting-state functional MRI signal." <u>Proc. Natl. Acad. Sci. U.S.A.</u> **104**(46): 18265-18269.

Magnuson, M., W. Majeed, et al. (2009). "Mapping functional connectivity in the anesthetized rat using CBV vs BOLD." <u>Proc. Int. Soc. Magn. Reson. Med. Sci. Meet. Exhib.</u> **17**: 1656.

Majeed, W., M. Magnuson, et al. (2009). "Spatiotemporal dynamics of low frequency fluctuations in BOLD fMRI of the rat." <u>J. Magn. Reson. Imaging.</u> **30**(2): 384-393.

Majeed, W., M. Magnuson, et al. (2009). "Stimulus induced modulation of low frequency fluctuations in BOLD fMRI of the rat." <u>Proc. Int. Soc. Magn. Reson. Med. Sci. Meet. Exhib.</u> **17**: 1581.

Mantini, D., M. Perrucci, et al. (2007). "Electrophysiological signatures of resting state networks in the human brain." <u>Proceedings of the National Academy of Sciences</u> **104**(32): 13170.

McNamara, A., M. Tegenthoff, et al. (2007). "Increased functional connectivity is crucial for learning novel muscle synergies." NeuroImage **35**(3): 1211-1218.

Obrig, H., M. Neufang, et al. (2000). "Spontaneous Low Frequency Oscillations of Cerebral Hemodynamics and Metabolism in Human Adults." NeuroImage **12**(6): 623-639.

Ogawa, S., T. Lee, et al. (1990). "Brain Magnetic Resonance Imaging with Contrast Dependent on Blood Oxygenation." Proceedings of the National Academy of Sciences **87**(24): 9868-9872.

Ostergaard, L., R. Weisskoff, et al. (1996). "High resolution measurement of cerebral blood flow using intravascular tracer bolus passages. Part I: Mathematical approach and statistical analysis." Magn Reson Med **36**(5): 715-25.

Pawela, C., B. Biswal, et al. (2008). "Resting-state functional connectivity of the rat brain." Magn Reson Med **59**(5): 1021–1029.

Peltier, S., C. Kerssens, et al. (2005). "Functional connectivity changes with concentration of sevoflurane anesthesia." NeuroReport **16**(3): 285.

Raichle, M., A. MacLeod, et al. (2001). "A default mode of brain function." Proceedings of the National Academy of Sciences **98**(2): 676.

Sakai, K., E. Watanabe, et al. (1995). "Functional mapping of the human somatosensory cortex with echo-planar MRI." Magnetic Resonance in Medicine **33**(5): 736-743.

Schölvinck, M., A. Maier, et al. (2010). "Neural basis of global resting-state fMRI activity." Proceedings of the National Academy of Sciences **107**(22): 10238.

Seeley, W. W., V. Menon, et al. (2007). "Dissociable intrinsic connectivity networks for salience processing and executive control." J. Neurosci. **27**(9): 2349-2356.

Shmuel, A. and D. Leopold (2008). "Neuronal correlates of spontaneous fluctuations in fMRI signals in monkey visual cortex: Implications for functional connectivity at rest." Hum Brain Mapp **29**: 751-761.

Silva, A., S. Lee, et al. (1999). "Simultaneous blood oxygenation level-dependent and cerebral blood flow functional magnetic resonance imaging during forepaw stimulation in the rat." J Cereb Blood Flow & Metab **19**: 871-879.

van de Ven, V., E. Formisano, et al. (2004). "Functional connectivity as revealed by spatial independent component analysis of fMRI measurements during rest." Hum. Brain. Mapp. **22**(3): 165-178.

Villalobos, M., A. Mizuno, et al. (2005). "Reduced functional connectivity between V1 and inferior frontal cortex associated with visuomotor performance in autism." NeuroImage **25**(3): 916-925.

Vincent, J., G. Patel, et al. (2007). "Intrinsic functional architecture in the anaesthetized monkey brain." Nature **447**(7140): 83.

Vincent, J., A. Snyder, et al. (2006). "Coherent spontaneous activity identifies a hippocampal-parietal memory network." J. Neurophysiol. **96**(6): 3517-3531.

Williams, K. A., M. Magnuson, et al. (in press). "Comparison of α-chloralose, medetomidine, and isoflurane anesthesia for functional connectivity mapping in the rat." Magn. Reson. Imaging.

Williams, K. A., S. J. Peltier, et al. (2006). "MRI evidence of resting state connectivity in rodent brain." Proc. Intl. Soc. Mag. Reson. Med. **14**: 2116.

Zhao, F., P. Wang, et al. (2005). "Spatial specificity of cerebral blood volume-weighted fMRI responses at columnar resolution." Neuroimage **27**(2): 416-424.

Zhao, F., T. Zhao, et al. (2008). "BOLD study of stimulation-induced neural activity and resting-state connectivity in medetomidine-sedated rat." NeuroImage **39**(1): 248-260.